Polar Ionospheric Response During Severe Geomagnetic Storms

A THESIS

Submitted in partial fulfillment of the
requirements for the awards of the degree
of
Master of Science

by

Vishal Sarkar



DEPARTMENT OF ASTRONOMY, ASTROPHYSICS & SPACE ENGINEERING

INDIAN INSTITUTE OF TECHNOLOGY INDORE

May 8, 2026

INDIAN INSTITUTE OF TECHNOLOGY INDORE

CANDIDATE'S DECLARATION

I hereby certify that the work which is being presented in the thesis entitled **"Polar Ionospheric Response During Severe Geomagnetic Storms"** in the partial fulfillment of the requirements for the award of the degree of **MASTER OF SCIENCE** and submitted in the **DEPARTMENT OF DAASE, Indian Institute of Technology Indore**, is an authentic record of my own work carried out during the time period from June, 2025 to May, 2026 under the supervision of Dr. Saurabh Das, Associate Professor. The matter presented in this thesis has not been submitted by me for the award of any other degree of this or any other institute.

Vishal Sarkar
08/05/26

Signature of the student with date
(Vishal Sarkar)

This is to certify that the above statement made by the candidate is correct to the best of my knowledge.

S. Das

8th May 2026

Signature of the Supervisor of

M.Sc. thesis (with date)

(Dr. Saurabh Das)

Vishal Sarkar has successfully given his/her M.Sc. Oral Examination held on **5 th May 2026**.

S. Das

Signature(s) of Supervisor(s) of MSc thesis
Date: 8th May 2026

Manoweta Chakraborty

Programme Coordinator, M.Sc.
Date: 08/05/2026

Manoweta Chakraborty

Convenor, DPGC
Date: 08/05/2026

S. Das

HoD, DAASE
Date:8th May 2026

Acknowledgement

I would like to express my sincere gratitude to the Indian Institute of Technology Indore for providing an excellent academic environment, along with essential resources such as library facilities, quality education, and a supportive space that encouraged both my research work and personal development.

I also acknowledge the Department of Astronomy, Astrophysics and Space Engineering (DAASE) for fostering a highly motivating and intellectually stimulating environment. I am grateful to the faculty members Dr. Manoneeta Chakraborty,Dr. Priyanka Singh,Dr. Deepika Bollimpalli, Dr. Abhirup Datta, Dr. Bhargav Vaidya, Dr. Suman Majumdar, Dr. Amit Shukla, Dr. Narendra Nath Patra, Dr. Soumavo Ghosh, whose teaching and guidance have been instrumental throughout my academic journey.

I am deeply thankful to my M.Sc. thesis supervisor, Dr. Saurabh Das, for trusting me with this work and for his constant guidance and support whenever I encountered challenges. Beyond academic mentorship, his encouragement, motivation, and personal support played a significant role in helping me stay focused and confident throughout this work.I would also like to acknowledge my M.Sc. batch of 2026 for their continuous academic and professional support, which greatly contributed to my learning experience.

Finally, I sincerely thank my lab members Miss Kavita, Miss Tamanna Singh, Miss Dizna James, Miss Parvathy Thankachy P, Miss Lakshya, Mr. Lekraj Saini, Mr. Vaibhav Tyagi, and Mr. Santanu Maity for their active assistance during lab hours and for maintaining a positive, collaborative, and motivating environment that made working in the lab both productive and enjoyable.

ABSTRACT

On 11 May 2024 at approximately 02:14 UT, ground-based broadcasting and two-way radio communications experienced severe disruption. The effect persisted for nearly two hours, resulting in operational delays in the aviation and maritime sectors, as well as disruptions to regional transportation systems. The global economic impact of this event is estimated to be on the order of billions of dollars.This disturbance was primarily driven by one of the most intense geomagnetic storms in the past two decades, and its consequent impact on ionospheric dynamics. In this paper, comparative analysis of three geomagnetic storms of varying intensities G5 (extreme), G3 (strong), and G2 (moderate) and investigate their effects on the ionosphere across different latitude regions.To achieve this,observational data were collected from three polar stations, three mid-latitude GNSS stations, and three equatorial GNSS stations in the Southern Hemisphere, while maintaining approximately constant longitude to minimize longitudinal variability.

During geomagnetic storms, high-energy charged particles enter the Earth's atmosphere predominantly through the polar cap regions. The resulting velocity difference between neutral particles in the thermosphere and the incoming charged particles leads to enhanced Joule heating and particle precipitation heating, causing the thermosphere to expand. This expansion increases the neutral density in the ionospheric region and reduces the O/N_2 ratio, thereby creating favorable conditions for ion-neutral chemical reactions. As a consequence, the recombination rate increases, leading to a significant depletion of plasma density in certain regions of the ionosphere.During November, the high-latitude region experiences continuous darkness, resulting in insufficient solar heating to expand the thermosphere; as a result, during the moderate November geomagnetic storm, an increase in plasma density is observed due to reduced recombination. In the equatorial region, solar heating drives the upward movement of plasma. Subsequently, due to the $\mathbf{E} \times \mathbf{B}$ drift, plasma is transported and accumulates in the equatorial ionization anomaly (EIA) region, typically between $\pm 15^\circ$ to $\pm 22^\circ$ magnetic latitude. Beyond this region, particularly at mid-latitudes, a decrease in TEC is observed, indicating plasma redistribution and coupling between low- and mid-latitude ionospheric regions.

This study systematically examines these effects across polar, mid-latitude, and equatorial regions, providing a comprehensive interpretation of ionospheric response to geomagnetic activity. Special emphasis is placed on the polar ionosphere, as this region is both highly sensitive to geomagnetic forcing and comparatively underexplored, despite increasing aviation and maritime activity along polar routes. Detailed analysis and observational evidence are presented to better understand the complex behavior of the polar ionosphere during geomagnetic disturbances.

Contents

List of Figures iii

List of Tables iii

1 Introduction 1

1.1 Vertical Structure of the Ionospheric Layers . . . 1
1.2 High Latitude Ionosphere and Auroral Light . . . 2
1.3 Effect of Geomagnetic Storm on Ionosphere . . . 3
1.3.1 Magnetic Reconnection . . . 3
1.3.2 Uplift of the Ionospheric F Region . . . 4
1.3.3 Equatorial Ionospheric Anomaly(EIA) . . . 5
1.4 Geomagnetic Storms . . . 6
1.5 Indication of Geomagnetic Storms . . . 6
1.5.1 SYM-H Index . . . 8
1.5.2 Kp Index . . . 8
1.5.3 AE, AU, and AL Indices . . . 9
1.5.4 IMF Components (Bt, Bx, By, Bz) . . . 9
1.5.5 Solar Wind Speed . . . 10
1.6 Proton Density . . . 11

2 TEC Calculation using GNSS 12

2.1 Pseudorange . . . 12
2.2 Combining Code and Carrier Measurements of pseudorange . . . 13
2.2.1 Measurement Equations . . . 13
2.2.2 Recursive Carrier Smoothing Filter . . . 15
2.3 Ionosphere group and phase delay . . . 16
2.4 TEC Calculation using Dual Frequency . . . 17

3 Data and Methodology 19

3.1 GNSS stations at different latitudes . . . 19

3.2 Methodology of our study . . . 20
3.3 EISCAT Analysis for Ion and Electron Temperature . . . 21
3.4 TIMED/GUVI and O/N_2 Ratio . . . 21
3.5 Geomagnetic Storm Parameters . . . 22

4 Results and Discussion **23**
4.1 Comparative Analysis of Geomagnetic Storm Parameters . . . 23
4.2 TEC profile of three geomagnetic stroms . . . 25
4.2.1 Ionospheric Response to the 10-11 May 2024 Geomagnetic Storm . . . 25
4.2.2 Ionospheric Response to the 10-11 October 2024 Geomagnetic Storm . . . 28
4.2.3 Ionospheric Response to the November 2025 Geomagnetic Storm . . . 30
4.3 Ion Temperature (T_i) and Electron Temperature (T_e) profile of three geomagnetic storms . 32
4.3.1 Analysis of Ion Temperature (T_i) and Electron Temperature (T_e) May 2024 magnetic Storm . . . 32
4.3.2 Analysis of Ion Temperature (T_i) and Electron Temperature (T_e) for the October 2024 Geomagnetic Storm . . . 34
4.3.3 Ion Temperature (T_i) and Electron Temperature (T_e) Profile of the November 2025 Geomagnetic Storm . . . 35
4.4 Ionospheric Composition Analysis of two different geomagnetic storm . . . 36
4.4.1 Ionospheric Composition Analysis Using GUVI O/N_2 Ratio of May 2024 magnetic storm . . . 36
4.4.2 Ionospheric Composition Analysis of the October 2024 magnetic storm . . . 38
4.5 Observed Electron Density from ESR . . . 39
4.6 Interpretation of the Outcomes . . . 39

List of Figures

1.1 This diagram explains the mechanism of magnetic reconnection(Kivelson and Russell 1995) . . . 3
1.2 The panels show how the altitude of the F2 peak changed as the storm developed.(Lee et al. 2025) . . . 4
1.3 These maps show how the electron density peaks (EIA crests) moved with time during the storm (Lee et al. 2025). . . . 5
1.4 The upstream solar wind data and geomagnetic indices during 10–13 May 2024. (a) Solar wind speed (black) and proton density (red); (b) solar wind dynamic pressure; (c) interplanetary magnetic field strength (Bt), Bx, By, and Bz components in geocentric solar magnetospheric coordinates; (d) auroral electrojet indices; (e) the Kp index (bar plot) and SYM-H index (black). Kp is shown in red for values ≥ 7, and in ruby for values ≥ 8 (Jin et al. 2025) . . . 7

2.1 This plot indicates the locking of code.Pseudorange Measurement(Farrell 2008) . . . 12
2.2 Carrier smoothed pseudoranges with different filter lengths (Misra and Enge 2002) . . . 16
2.3 GNSS Stations help to calculate TEC accurately ,they also help to mitigate satellite errors (Montenbruck, Gill, and Lutze 2002) . . . 18

3.1 These are the locations of all the GNSS stations we have used to calculate TEC. . . . 19

4.1 Important parameters of the magnetic storm,where panel (a-c) describes important magnetic storm parameter from 10-11 may 2024 magnetic storm.Panel (d-f) explain important storm parameter from magnetic storm 10-11 october 2024 and the panel (g-i) represent storm parameter from magnetic storm 12-13 november 2025. Figure (a,d,g) represent SYM-H index and KP index,Panel (b,e,h) solar wind speed and proton density variation,figure(c,f,i) represent Auroral variation. . . . 24

4.2 This figure represent TECU variation on May 2024 magnetic storm at all the nine GNSS stations,panel (a-c) represent High latitude region,panel (d-f) represent equatorial region, and from (g-i) represent mid-Latitude.Beginning of the magnetic storm and the start of recovery phase is represented by black dotted line.Black curve represent the average storm day and Blue line represent IRI TEC prediction and red curve represent storm time TEC. 26
4.3 This figure represent TECU variation on October 2024 magnetic storm at all the nine GNSS stations,panel (a-c) represent High latitude region,panel (d-f) represent equatorial region, and from (g-i) represent mid-Latitude.Beginning of the magnetic storm and the start of recovery phase is represented by black dotted line.Black curve represent the average storm day and Blue line represent IRI TEC prediction and red curve represent storm time TEC. 28
4.4 This figure represent TECU variation on November 2025 magnetic storm at all the nine GNSS stations, panel (a-c) represent High latitude region, panel (d-f) represent equatorial region, and from (g-i) represent mid-Latitude. Beginning of the magnetic storm and the start of recovery phase is represented by black dotted line.Black curve represent the average storm day and Blue line represent IRI TEC prediction and red curve represent storm time TEC. 31
4.5 This figure represent time series plot of T_i and T_e , figure (p) represent temperature variation on day 10 May, (q) represent variation for temperature on the day 11 may and (r) represent temperature variation on 12 may 33
4.6 This figure represent time series plot of T_i and T_e ,figure (i) represent temperature variation on day 10 October,(j) represent variation for temperature on the day 11 October and (k) represent temperature variation on 14 October. 34
4.7 This figure represent time series plot of T_i and T_e ,figure (a) represent temperature variation on day 11 November,(b) represent variation for temperature on the day 12 November and (c) represent temperature variation on 13 November(Credit :https://portal.eiscat.se/) . . 35
4.8 GUVI data represent latitude longitude variation of O/N_2 ratio, figure (p) represent 10 May, figure (q) represent 11 may, and 12 May is represented by figure (r). 37
4.9 GUVI data represent latitude longitude variation of O/N_2 ratio, figure (a) represent 10 October, figure (b) represent 11 October, and 14 October is represented by figure (c). . . 38
4.10 Electron density observation form the ESR,panel (a) represent 7 november (b) represent 12 november (c) represent observation from 14 November(Credit :https://portal.eiscat.se/). 39

List of Tables

3.1 List of selected GNSS stations with their geographical coordinates and locations. 20

4.1 Major geomagnetic storms, their onset and beginning of the recovery phase 25

CHAPTER 1

INTRODUCTION

Understanding how solar activity shapes the near earth environment is a central theme in modern space physics research.Historical observations most notably the 1859 Carrington Event first revealed the profound impact that solar flares and associated ejections can have on geomagnetic conditions at Earth.These interactions manifest as geomagnetic storms.The Sun through its continuously evolving magnetic field and eruptive phenomena, drives a complex chain of plasma interactions that extend throughout the heliosphere and ultimately influence Earth's ionosphere.

The ionosphere is a highly ionized region of Earth's upper atmosphere, extending from approximately 60 km to nearly 1000 km, where solar ultraviolet and X-ray radiation ionize atmospheric particles and create a dynamic plasma environment essential for radio communication, satellite signal transmission, and space-weather interactions. Although it is an integral part of the atmosphere, its existence was confirmed only in the early twentieth century through the pioneering work of researchers such as Heaviside, Kennelly, and later Appleton, who demonstrated that radio waves could reflect from an electrically charged atmospheric layer ,it is a discovery that revolutionized long-distance communication. Today, the ionosphere is recognized as a variable and highly responsive atmospheric region influenced by solar activity, geomagnetic storms, and coupling with the lower atmosphere, making its study crucial for understanding and mitigating disruptions to modern technological systems.

1.1 Vertical Structure of the Ionospheric Layers

The ionosphere is structured into several distinct layers,the D, E, F1, and F2 regions ,each region is characterized by differing degrees of ionization, dominant chemical species, and altitude ranges within the upper atmosphere. The D layer (60–90 km) is the lowest and least ionized region, where high atmospheric density leads to rapid recombination, causing low-frequency

radio waves to be absorbed rather than reflected. Above it lies the E layer (90-140 km), where photoionization of molecular oxygen produces moderate electron densities capable of reflecting medium-frequency signals. Then there is F region, composed of the F1 (150-200 km) and F2 (200-400+ km) layers, contains the highest electron densities due to intense solar radiation and reduced recombination rates at these altitudes. The F2 layer, which persists even during nighttime, is the most important for long-distance high-frequency radio propagation (Kelley 2009).

The formation of these ionospheric layers is governed primarily by solar radiation and the altitude-dependent composition of the upper atmosphere (Kivelson and Russell 1995). Extreme ultraviolet (EUV) and X-ray photons ionize molecular and atoms, while the balance between ionization and recombination determines the strength and persistence of each layer (Koskinen 2011). The D and E regions show strong diurnal variability because higher atmospheric density enhances recombination, whereas the F region remains more stable owing to lower densities and continuous ion production supported by diffusion and transport processes. These mechanisms produce the stratified structure of the ionosphere and demonstrate its crucial role in radio communication and space-weather interactions.

1.2 High Latitude Ionosphere and Auroral Light

The high-latitude ionosphere, encompassing the polar caps and auroral zones, differs markedly from mid and low-latitude regions due to its direct magnetic connectivity to the solar wind through open magnetic field lines. In these regions, solar-wind energy is transferred into the magnetosphere with high efficiency, producing strong particle precipitation, intense ionospheric currents, and large plasma convection patterns across the polar cap. During geomagnetic storms, enhanced solar-wind electric fields drive rapid plasma transport, expressed as an increased cross-polar cap potential. The polar ionosphere also exhibits irregular electron density structures, severe scintillation of radio signals, and rapid temporal variability, making it one of the most challenging environments for communication and navigation technologies (Kivelson and Russell 1995).

Auroral light production in the high-latitude ionosphere results from the precipitation of energetic electrons and ions from the magnetosphere into the upper atmosphere along geomagnetic field lines (Mitra 1951). Collisions between these charged particles and atmospheric species such as atomic oxygen and molecular nitrogen excite the neutrals to higher energy states (Kelley 2009). As the excited atoms and molecules return to their ground states, they emit photons at

characteristic wavelengths, producing visible aurora. Green emissions (557.7 nm) arise from excited atomic oxygen at approximately 100–150 km, while red emissions (630.0 nm) originate from higher-altitude oxygen. Molecular nitrogen and its ions contribute blue and purple hues. This particle-precipitation mechanism directly links magnetospheric dynamics to optical emissions observed in the ionosphere.

1.3 Effect of Geomagnetic Storm on Ionosphere

Geomagnetic storms significantly disturb the ionosphere by altering electron density, enhancing particle precipitation, and intensifying ionospheric currents.Because of magnetic reconnection more charge particles than normal days enter ionosphere .This phenomenon is discussed below.Due to geomagnetic storms some interesting phenomenon can be noticed in the ionosphere like the increase in height of ionospheric F region,Expansion of Equatorial Ionospheric Anomaly which we have discusse below.

1.3.1 Magnetic Reconnection

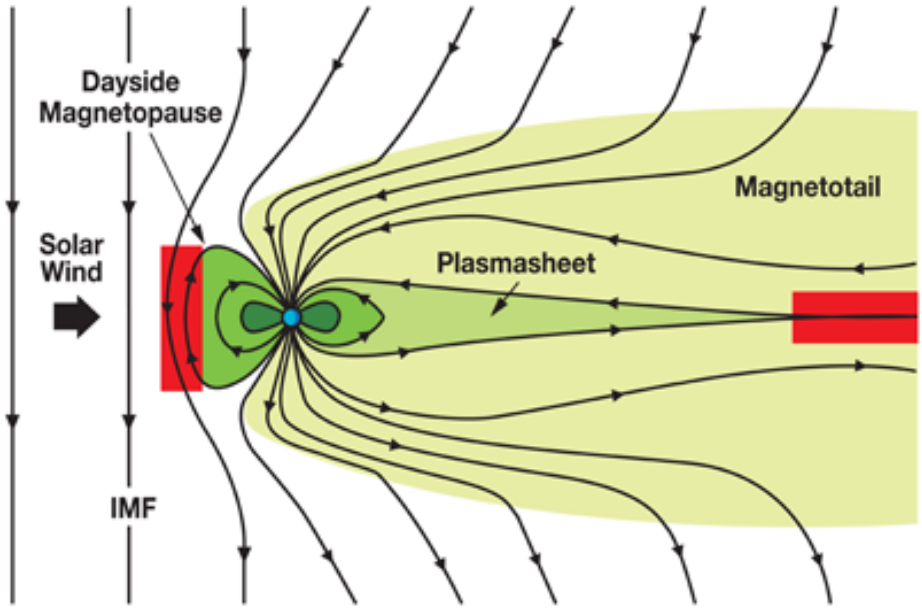

Figure 1.1: This diagram explains the mechanism of magnetic reconnection(Kivelson and Russell 1995)

Magnetic reconnection is the fundamental process that enables solar-wind energy, mass, and momentum to enter Earth's magnetosphere (Mitra 1951). During geomagnetic storms, when the interplanetary magnetic field (IMF) turns strongly southward, it becomes anti-parallel to Earth's northward dayside magnetic field, creating ideal conditions for reconnection at the

magnetopause (Cumnock 1994). This process breaks and merges magnetic field lines, forming newly connected lines that channel solar-wind plasma into the magnetosphere (Cumnock 1994). Under sustained southward B_z, the reconnection rate increases dramatically, allowing large-scale energy transfer that compresses the dayside magnetosphere, enhances global convection, and initiates the buildup of plasma and magnetic stress in the magnetotail (Fuselier, Petrinec, and Trattner 2000).

As solar-wind energy accumulates in the magnetotail, magnetic field lines are stretched and loaded with plasma. Eventually, tail reconnection occurs, releasing stored energy explosively and injecting energetic particles toward Earth. These injections intensify the ring current, disturb ionospheric currents, and trigger auroral activity, which together form the primary signatures of a geomagnetic storm (Koskinen 2011). The combined action of dayside and tail reconnection governs storm onset, main-phase evolution, and ionospheric disturbances, making magnetic reconnection the central mechanism linking solar-wind variability to geomagnetic storm dynamics.

1.3.2 Uplift of the Ionospheric F Region

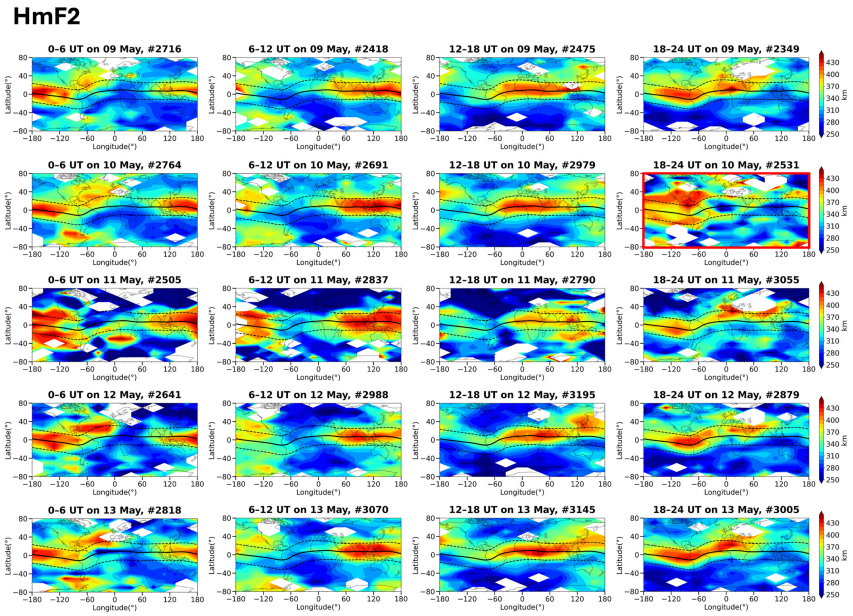

Figure 1.2: The panels show how the altitude of the F2 peak changed as the storm developed.(Lee et al. 2025)

The uplift of the ionospheric F region, particularly near the magnetic equator, is primarily driven by enhanced postsunset upward $\mathbf{E} \times \mathbf{B}$ drift (Lee et al. 2025), which elevates the peak electron density (the F_2 peak) to higher altitudes where recombination rates are significantly lower. This vertical transport increases the plasma content over a wider altitude range and modifies the

distribution of TEC, often producing enhanced TEC during the early evening hours. The uplift further intensifies the formation of the Equatorial Ionization Anomaly (EIA) (Lee et al. 2025), by raising plasma to heights where it can diffuse along magnetic field lines toward the anomaly crests. Thus, the rise of the F region plays a central role in preconditioning the ionosphere for irregularity formation.

Changes in the altitude and structure of the F region exert a strong influence on radio-wave propagation. Increased TEC resulting from F-region uplift introduces phase delays and range errors in GNSS observations, while steep TEC gradients distort signal paths and degrade positioning accuracy. Moreover, when uplift conditions become excessive, they enhance the likelihood of irregularity formation and ionospheric scintillation, leading to amplitude fading, phase fluctuations, and temporary loss of lock on satellite signals. Therefore, F-region uplift functions both as a precursor and a direct contributor to radio-signal degradation in equatorial regions.

1.3.3 Equatorial Ionospheric Anomaly(EIA)

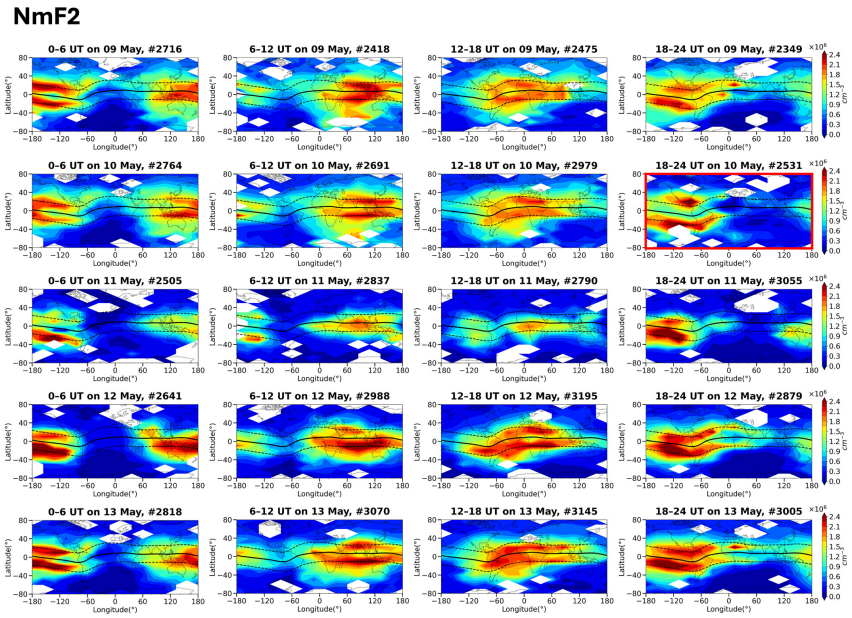

Figure 1.3: These maps show how the electron density peaks (EIA crests) moved with time during the storm (Lee et al. 2025).

The Equatorial Ionospheric Anomaly (EIA) is a prominent large-scale structure of the low-latitude ionosphere, characterized by two enhanced electron-density crests located approximately 15°–20° north and south of the magnetic equator. The formation of the EIA is governed by the equatorial fountain effect (Lee et al. 2025), which is driven by the upward daytime $\mathbf{E} \times \mathbf{B}$ drift. During daytime, strong solar heating and ionization enhance the eastward electric field,

lifting ionospheric plasma from the equatorial F-region to higher altitudes where recombination rates are significantly reduced. Once elevated, gravity and pressure-gradient forces transport the plasma poleward along geomagnetic field lines, producing the characteristic double-crest structure of the anomaly.

1.4 Geomagnetic Storms

Geomagnetic storms originate from explosive or rapidly evolving solar processes that restructure the Sun's magnetic field. The two primary drivers are coronal mass ejections (CMEs) and high-speed solar-wind streams (HSSs) (Koskinen 2011). CMEs occur when magnetic energy stored in the solar corona is suddenly released, ejecting massive clouds of magnetized plasma into interplanetary space. These structures often carry strong, coherent magnetic fields capable of interacting intensely with Earth's magnetosphere (Mitra 1951). High-speed streams arise from coronal hole regions of open magnetic field lines,which accelerate plasma outward and create recurrent solar-wind disturbances (Kivelson and Russell 1995). Both mechanisms generate large-scale variations in solar-wind velocity, density, and magnetic-field orientation, forming the fundamental storm-driving structures in the heliosphere.

After their launch, CMEs and high-speed streams propagate through the heliosphere and eventually encounter Earth. When the embedded magnetic field exhibits a southward B_z orientation, magnetic reconnection at the dayside magnetopause becomes highly efficient, allowing solar-wind energy to enter the magnetosphere (Curto 2020). This drives ring-current intensification, enhances magnetospheric convection, and strengthens auroral-zone currents, producing the magnetic-field depressions and ionospheric disturbances characteristic of geomagnetic storms. The severity of the storm depends on the speed, density, and magnetic-field structure of the solar-wind driver.

1.5 Indication of Geomagnetic Storms

Geomagnetic storms are characterized and monitored through a set of key parameters that capture different aspects of the Sun Earth interaction. The Kp index provides a global measure of geomagnetic disturbance by summarizing mid-latitude magnetic variability over three-hour intervals, making it one of the most widely used storm-intensity indicators. The SYM-H index, a high-resolution counterpart of Dst, quantifies the symmetric ring-current strength and offers minute-scale insight into storm phases, especially the rapid main-phase depression of

the geomagnetic field. High-latitude currents are represented by the AE index, which reflects the intensity of the auroral electrojets driven by magnetosphere–ionosphere coupling and substorm activity. On the solar-wind side, parameters such as solar-wind velocity, proton density, dynamic pressure, and the interplanetary magnetic field (IMF)particularly its southward B_z component control the efficiency of energy transfer into the magnetosphere. High solar-wind speeds, elevated density, and strong southward IMF greatly enhance magnetospheric compression and reconnection, intensifying geomagnetic responses. Together, these parameters provide a comprehensive description of storm drivers, magnetospheric response, and ionospheric electrodynamics, making them essential for diagnosing and interpreting geomagnetic storm events.Detailed Description of all this parameter are given below (Koskinen 2011).

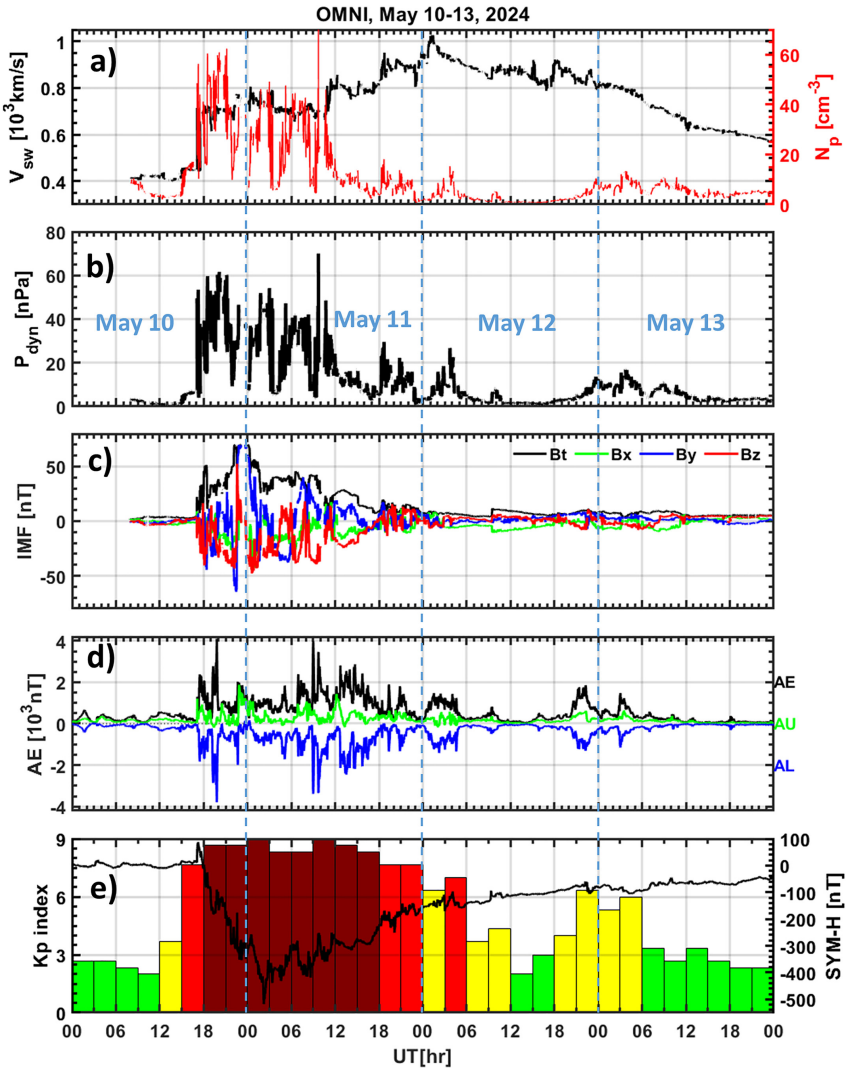

Figure 1.4: The upstream solar wind data and geomagnetic indices during 10–13 May 2024. (a) Solar wind speed (black) and proton density (red); (b) solar wind dynamic pressure; (c) interplanetary magnetic field strength (Bt), Bx, By, and Bz components in geocentric solar magnetospheric coordinates; (d) auroral electrojet indices; (e) the Kp index (bar plot) and SYM-H index (black). Kp is shown in red for values ≥ 7, and in ruby for values ≥ 8 (Jin et al. 2025)

.

The fig 1.4 shows variation in important storm parameters .This variations are recorded durind the geomagneric which occured on 10-13 may 2024 ,which is one of the strongest storm in two decades.

1.5.1 SYM-H Index

The SYM-H index provides a high-resolution (1-minute) measure of the global depression of the horizontal geomagnetic field during geomagnetic storms. It represents the symmetric component of storm-time magnetic disturbances and serves as a refined version of the Dst index. Negative excursions in SYM-H directly indicate the strengthening of the symmetric ring current, making it a key parameter for quantifying storm intensity and temporal evolution.

SYM-H is derived from low-latitude ground magnetometers distributed longitudinally. Each station records the horizontal magnetic field component (H), and quiet-time variations along with non–ring-current contributions are removed. The corrected values from all stations are subsequently averaged to isolate the longitudinally symmetric disturbance. This averaging suppresses local and asymmetric contributions including partial ring currents and ionospheric currents yielding a clean measure of the global magnetospheric response.

The depression captured by SYM-H originates from the storm time symmetric ring current (Picanço et al. 2024), produced when energetic ions and electrons injected during periods of southward IMF drift around Earth under curvature- and gradient-drift forces. The enhanced westward current weakens Earth's magnetic field uniformly, and this reduction is precisely what the SYM-H index tracks.

1.5.2 Kp Index

The Kp index provides a global measure of geomagnetic disturbance by quantifying irregular variations in the horizontal magnetic field at mid-latitude stations. It summarizes the overall level of geomagnetic activity over three-hour intervals using a quasi-logarithmic scale ranging from 0 to 9. Rather than isolating a single current system, Kp reflects the combined response of multiple magnetospheric and ionospheric current systems driven by solar-wind variability, making it a broad and widely used indicator of storm intensity.

Kp is constructed from magnetometer observations at a standardized network of mid-latitude stations distributed across multiple longitudes. Each station computes a local disturbance value based on deviations of the horizontal field from quiet-day baselines. These local values

are normalized to account for station-specific magnetic characteristics, and the normalized disturbances are combined to produce the final planetary index. The use of mid-latitude stations minimizes contamination from the highly variable auroral zone while still capturing the global geomagnetic response.

The variations detected by the Kp index arise from a complex interplay of current systems generated by solar-wind–magnetosphere coupling. Enhanced solar-wind speed, density, and strong southward IMF promote magnetic reconnection, energizing processes such as auroral electrojets, field-aligned currents, the partial ring current, and magnetopause currents. These dynamic current systems perturb the magnetic field at mid-latitudes, and their cumulative effect is reflected through elevated Kp values.

1.5.3 AE, AU, and AL Indices

The AE, AU, and AL indices quantify the strength and dynamics of ionospheric currents flowing in the auroral region. The AU index represents the intensity of the eastward auroral electrojet, whereas the AL index reflects the strength of the westward electrojet. The AE index, defined as AU minus AL, captures the total range of auroral current variability and therefore serves as a measure of substorm activity and high-latitude electrodynamic disturbances.

AE, AU, and AL are derived from a longitudinal chain of high-latitude ground magnetometers known as the auroral electrojet network. Each station records perturbations in the horizontal magnetic field produced by ionospheric currents flowing above. The maximum positive deviation among stations defines AU, the maximum negative deviation defines AL, and their difference yields AE. This configuration provides continuous monitoring of auroral electrodynamics and separates eastward and westward current contributions.

Auroral electrojets arise when solar-wind energy is transferred into the magnetosphere and subsequently released into the ionosphere through field-aligned currents. Enhanced particle precipitation and increased ionospheric conductivity during substorms allow strong currents to form: the eastward electrojet dominates in the morning sector, while the westward electrojet intensifies in the evening sector. Their combined variability, driven by magnetotail reconnection and plasma injections, is what the AE index captures.

1.5.4 IMF Components (Bt, Bx, By, Bz)

The interplanetary magnetic field (IMF) represents the magnetic field carried by the solar wind throughout interplanetary space. The scalar field strength Bt denotes the total IMF magnitude, while the vector components Bx, By, and Bz describe its orientation in geocentric solar magnetospheric (GSM) coordinates. Among these, Bz is the most critical for geomagnetic

storm development because a southward (negative) Bz orientation enables efficient solar-wind energy transfer into Earth's magnetosphere via magnetic reconnection.

IMF parameters are measured by magnetometers onboard upstream spacecraft such as ACE, DSCOVR, and Wind, located near the L1 Lagrangian point, where they sample undisturbed solar wind before it encounters Earth. These spacecraft provide high-resolution vector magnetic field measurements, which are then transformed into GSM coordinates. The observations are propagated forward to estimate the field conditions impacting the magnetosphere, allowing real-time monitoring of IMF variability and storm-driving features.

IMF disturbances arise from solar phenomena such as coronal mass ejections, high-speed solar wind streams, and interaction regions formed by colliding plasma flows. These structures modify both the magnitude and orientation of the embedded magnetic field. When such IMF structures interact with Earth, particularly when Bz turns southward, they enhance magnetic reconnection and drive energization of current systems throughout the magnetosphere and ionosphere. Thus, the IMF components govern the primary drivers of geomagnetic storm dynamics.

1.5.5 Solar Wind Speed

Solar wind speed quantifies the velocity of the continuous stream of charged particles primarily protons and electrons flowing outward from the Sun and arriving at Earth. It is a fundamental parameter controlling solar wind magnetosphere coupling, as higher solar wind speeds increase the dynamic pressure on the magnetosphere, compressing it and enabling more efficient energy transfer during geomagnetic storms. Variations in solar wind speed significantly influence magnetospheric convection, substorm initiation, and the overall level of geomagnetic disturbance.

Proton density is determined by plasma instruments aboard on spacecraft same as IMF ones.These instruments detect the flux of incoming ions and derive the bulk flow velocity from particle momentum distributions. The measurements are transmitted in near real time and propagated to estimate when solar wind structures will reach the magnetosphere. Continuous monitoring enables accurate tracking of high-speed streams, shock fronts, and transient structures that drive geomagnetic activity.

Variations in solar wind speed arise from different solar sources. High-speed streams originate from coronal holes, while extremely fast flows accompany coronal mass ejections and interplanetary shock fronts. Interaction regions between slow and fast solar wind create compressed, turbulent plasma structures that enhance geoeffectiveness. When these varying-speed flows impact Earth, they modulate magnetospheric dynamics and strongly influence geomagnetic storm development.

1.6 Proton Density

Proton density quantifies the number of solar-wind protons per unit volume, typically expressed in particles per cubic centimeter. It is a key parameter that governs the mass flux and dynamic pressure of the solar wind, both of which strongly influence the size and configuration of Earth's magnetosphere. Elevated proton density increases solar-wind pressure, leading to magnetospheric compression, enhanced convection, and a more pronounced geomagnetic response during storms.

Proton density is also determined by plasma instruments aboard on spacecraft same as previous ones. These instruments measure particle count rates and velocity distributions, from which the proton number density is derived. Continuous monitoring of proton density provides early warnings of high-pressure solar-wind intervals and allows prediction of magnetospheric compression and storm intensification (Koskinen 2011).

Variations in proton density arise from solar structures with differing plasma characteristics. High-density streams are commonly associated with coronal mass ejections, compression regions, and interplanetary shocks, while low-density plasma originates from coronal holes and rarefaction regions. When dense solar-wind plasma interacts with Earth's magnetosphere, it increases the solar-wind dynamic pressure and strengthens magnetopause currents, contributing significantly to geomagnetic storm development.

CHAPTER 2

TEC Calculation using GNSS

The GNSS (Global Navigation Satellite System) came into existence with the invention of GPS. GPS was developed by the U.S. Department of Defence in the 1970s for military navigation and missile guidance. It was only made available for civilian use in the 1980s. Each GPS satellite has atomic clocks accurate to one-billionth of a second, ensuring pinpoint precision in location calculations.

2.1 Pseudorange

The pseudorange is a biased estimate of the true geometric range between the satellite and the user (Farrell 2008). As shown in the figure 2.1, the satellite and receiver clocks are not synchronized, additional terms are included to model delays and errors in the measurement. Equation 2.0 expresses the measured pseudorange as

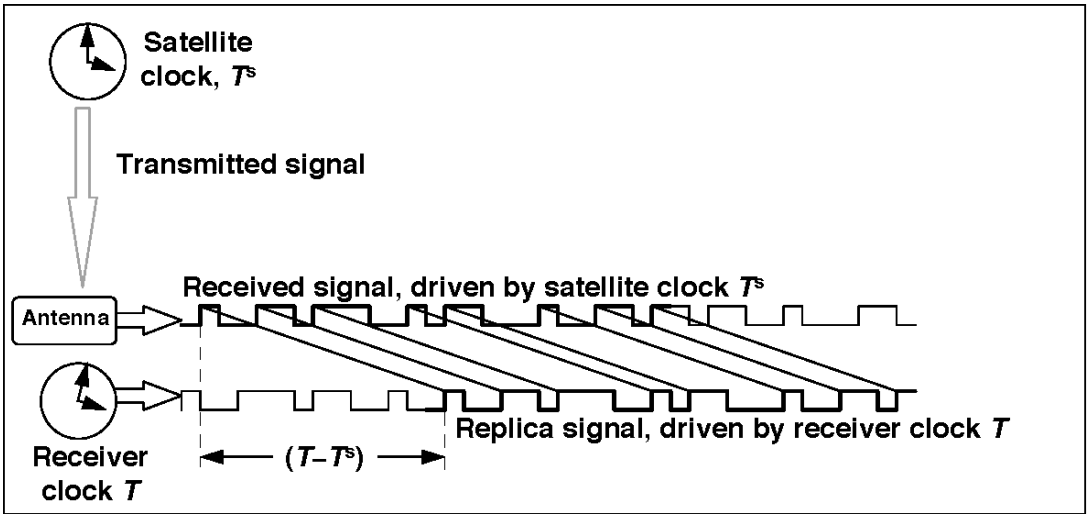

Figure 2.1: This plot indicates the locking of code.Pseudorange Measurement(Farrell 2008)

$$\rho = r + c(\delta t_u - \delta t^s) + I_p + T_p + \varepsilon_p, \tag{2.0}$$

where r is the true geometric range, c is the speed of light, δt_u is the receiver clock bias, and δt^s is the satellite clock bias (Misra and Enge 2002). The terms I_p and T_p denote ionospheric and tropospheric delays, which increase the apparent range. The final term ε_p represents measurement noise and other unmodeled effects. Since the receiver cannot directly measure the true range r, it relies on repeated pseudorange measurements from multiple satellites to estimate user position, velocity, and time while compensating for these biases.

2.2 Combining Code and Carrier Measurements of pseudorange

Carrier phase measurements in GPS offer very high precision centimeter level, but they suffer from an inherent ambiguity due to the unknown integer number of cycles. On the other hand, code-based pseudorange measurements are unambiguous but noisy meter level (Singh and Tiwari 2022). This section discusses how to combine both measurements to obtain accurate and reliable positioning.

2.2.1 Measurement Equations

The code pseudorange measurement is given by (Misra and Enge 2002):

$$\rho(t) = r(t) + c[\delta t_u(t) - \delta t^s(t-\tau)] + I(t) + T(t) + \epsilon_\rho(t) \tag{2.1}$$

The carrier phase pseudorange measurement is:

$$\Phi(t) = r(t) + c[\delta t_u(t) - \delta t^s(t-\tau)] - I(t) + T(t) + \lambda N + \epsilon_\Phi(t) \tag{2.2}$$

where:

- $r(t)$: geometric range
- c: speed of light
- δt_u, δt^s: receiver and satellite clock errors
- $I(t)$: ionospheric delay
- $T(t)$: tropospheric delay

- λ: wavelength
- N: integer ambiguity
- ϵ: measurement noise

$$\rho_{IF}(t) = r(t) + c[\delta t_u(t) - \delta t^s(t - \tau)] + T(t) \tag{2.3}$$

Then:

$$\rho(t) = \rho_{IF}(t) + I(t) + \epsilon_\rho(t) \tag{2.4}$$

$$\tag{2.5}$$

$$\Phi(t) = \rho_{IF}(t) - I(t) + \lambda N + \epsilon_\Phi(t) \tag{2.6}$$

Between two epochs t_{i-1} and t_i:

$$\Delta\rho(t_i) = \rho(t_i) - \rho(t_{i-1}) \qquad = \Delta\rho_{IF}(t_i) + \Delta I(t_i) + \Delta\epsilon_\rho(t_i) \tag{2.7}$$

$$\Delta\Phi(t_i) = \Phi(t_i) - \Phi(t_{i-1}) \qquad = \Delta\rho_{IF}(t_i) - \Delta I(t_i) + \Delta\epsilon_\Phi(t_i) \tag{2.8}$$

Carrier phase provides a very precise estimate of $\Delta\rho_{IF}$, since ambiguity cancels out in the difference (Misra and Enge 2002).

Carrier Smoothing Concept

An estimate of the initial pseudorange can be formed as:

$$\hat{\rho}(t_0)_i = \rho(t_i) - [\Phi(t_i) - \Phi(t_0)] \tag{2.9}$$

Averaging over n epochs:

$$\bar{\rho}(t_0) = \frac{1}{n}\sum_i \hat{\rho}(t_0)_i \tag{2.10}$$

Reconstructing the smoothed pseudorange:

$$\bar{\rho}(t_i) = \bar{\rho}(t_0) + [\Phi(t_i) - \Phi(t_0)] \tag{2.11}$$

2.2.2 Recursive Carrier Smoothing Filter

A practical implementation of carrier smoothing is given by the recursive filter (Singh and Tiwari 2022):

$$\bar{\rho}(t_i) = \frac{1}{M}\rho(t_i) + \frac{M-1}{M}\left[\bar{\rho}(t_{i-1}) + (\Phi(t_i) - \Phi(t_{i-1}))\right] \tag{2.12}$$

where M represents the smoothing window length.

Meaning of Symbols

- $\bar{\rho}(t_i)$ Smoothed pseudorange at the current epoch. This is the final improved estimate.
- $\rho(t_i)$ Raw code pseudorange measurement at time t_i. It is noisy (meter-level) but provides absolute distance.
- $\bar{\rho}(t_{i-1})$ Previously smoothed pseudorange. It is already filtered and more reliable than raw code.
- $\Phi(t_i) - \Phi(t_{i-1})$ Carrier phase change between two epochs. This term is extremely precise (centimeter-level) and represents the change in range.
- M Smoothing window length, controlling the balance between code and carrier contributions.

The carrier smoothing filter effectively combines the strengths of both measurements Figure 2.2.Code measurements provide absolute positioning.Carrier phase measurements provide high precision.This approach significantly improves the quality of pseudorange measurements.

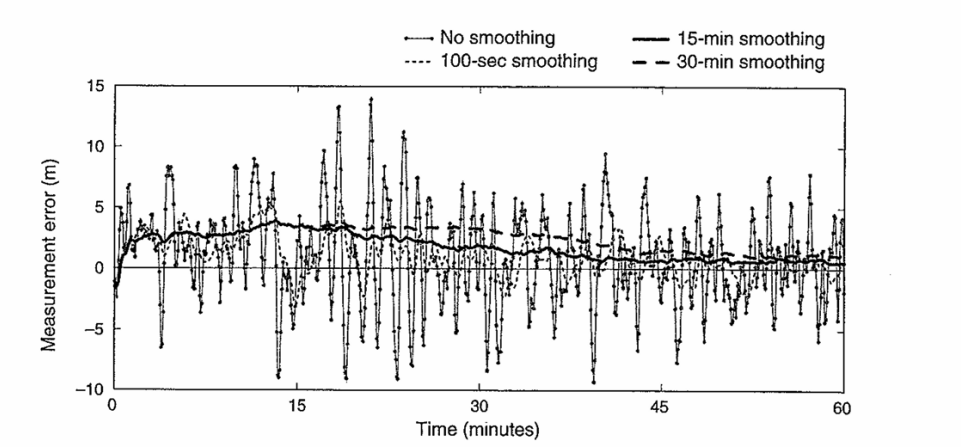

Figure 2.2: Carrier smoothed pseudoranges with different filter lengths (Misra and Enge 2002)

.

Combining code and carrier measurements allows the strengths of both to be utilized. Code measurements provide absolute range.This combination significantly improves positioning accuracy.

2.3 Ionosphere group and phase delay

The speed of a radio signal in the ionosphere depends on the number of free electrons encountered along its path.The total electron content (TEC) is defined as (Misra and Enge 2002):

$$TEC = \int_s^R n_e(l)\, dl,$$

where $n_e(l)$ is the electron density along the signal path from the satellite (R) to the receiver (s). TEC is measured in TEC units (TECU), where 1 TECU = 10^{16} electrons/m^2. Ionized gas is a dispersive medium, and the refractive index for a radio wave of frequency f is approximated by

$$n_p = 1 - \frac{40.3\, n_e}{f^2}. \tag{2.13}$$

The excess phase delay accumulated through the ionosphere is

$$\Delta\tau_p = \frac{1}{c}\int_s^R (n_p - 1)\, dl = -\frac{1}{c}\int_s^R \frac{40.3\, n_e(l)}{f^2}\, dl = -\frac{40.3\, TEC}{c f^2}.$$

The negative sign indicates that the carrier phase is advanced. The corresponding phase delay

in meters is

$$I_\phi = c\Delta\tau_p = -\frac{40.3\,TEC}{f^2}. \tag{2.14}$$

Similarly, the group refractive index is

$$n_g = 1 + \frac{40.3\,n_e}{f^2},$$

and the corresponding group delay (pseudorange delay) is

$$I_\rho = \frac{40.3\,TEC}{f^2}.$$

The ionospheric delay for code measurements and carrier phase measurements have equal magnitude and opposite sign:

$$I_\rho = -I_\phi = \frac{40.3\,TEC}{f^2}. \tag{2.15}$$

Thus, the code (group) signal is delayed, while the carrier phase is advanced (Singh and Tiwari 2022).

2.4 TEC Calculation using Dual Frequency

Dual-frequency GPS measurements allow estimation and mitigation of ionospheric delay, which is the largest error source affecting GPS signals. Since the ionospheric effect varies approximately as $1/f^2$, observations at two different frequencies (L1 and L2) enable separation of geometric range from ionospheric contribution (Hofmann-Wellenhof, Lichtenegger, and Collins 2012).

For a given frequency f_q (with q = L1 or L2), the pseudorange measurement is

$$\rho_q = r + c(\delta t_u - \delta t^s) + I_q + T + \varepsilon_{\rho_q},$$

where r is geometric range, T the tropospheric delay, $I_q = \frac{40.3\,TEC}{f_q^2}$ the ionospheric group delay, δt_u and δt^s the clock biases, and ε_{ρ_q} measurement noise.
Since the ionospheric delay varies with $1/f^2$, the model can be rewritten as

$$\rho_q = \rho_{IF} + \frac{A}{f_q^2},$$

where ρ_{IF} is the ionosphere-free pseudorange and $A = 40.3\,TEC$.
Using dual-frequency pseudoranges at L1 and L2, an estimate of L1 ionospheric delay is

$$I_{L1} = \frac{A}{f_{L1}^2} = \frac{f_{L2}^2}{(f_{L1}^2 - f_{L2}^2)}(\rho_{L2} - \rho_{L1}). \tag{2.16}$$

Eliminating ionospheric delay yields Numerically, this becomes

$$TEC = \frac{f_{L2}^2 f_{L1}^2}{(f_{L1}^2 - f_{L2}^2)40.3}(\rho_{L2} - \rho_{L1}). \tag{2.17}$$



Figure 2.3: GNSS Stations help to calculate TEC accurately ,they also help to mitigate satellite errors (Montenbruck, Gill, and Lutze 2002)

.

From the equation(1.5) (Misra and Enge 2002) we can calculate the TEC value ,with the help of pseudorange at L1 and L2 and the frequency of L1 and L2 band. The parameter TEC is very important as it is directly related to ionospheric delay ,and it also help to model any type of radio signal through ionosphere figure (2.3).TEC also help us understand ionospheric anomalies when it interacts with major solar storms.

CHAPTER 3

Data and Methodology

3.1 GNSS stations at different latitudes

All selected stations are located near the zero degree meridian, including three stations in the high-latitude polar region: TRO100NOR, NYA100NOR, and SCOR00GRL; three stations near the equatorial region: YKRO00CIV, NKLG00GAB, and ASCG00SHN; and three stations in the Southern Hemisphere: WIND00NAM,ZAMB00ZMB, SUTH00ZAF, and JCTW00ZAF. The figure 3.1 shows the loaction of all the GNSS Stations whose data we have used in our study.

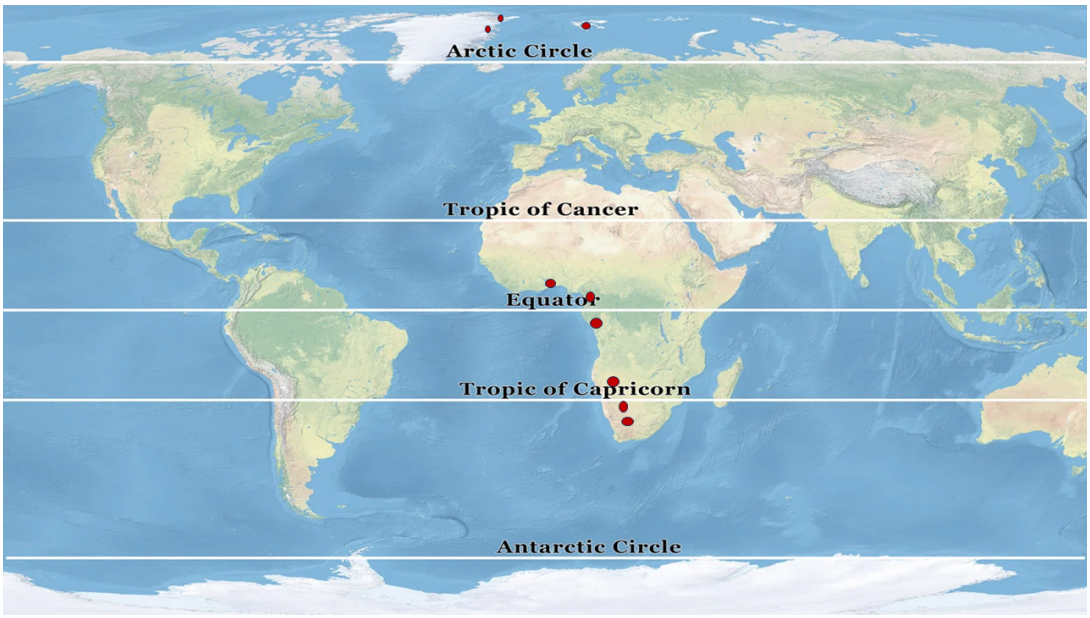

Figure 3.1: These are the locations of all the GNSS stations we have used to calculate TEC.

Station code	Longitude	Latitude	Country
TRO100NOR (N pole)	18.940	69.663	Tromsø, Norway
NYA100NOR (N pole)	11.865	78.930	Ny-Ålesund
SCOR00GRL (N pole)	-21.950	70.485	Greenland
YKRO00CIV (equ)	-5.240	6.871	Yamoussoukro
NKLG00GAB (equ)	9.672	0.354	Gabon
ASCG00SHN (equ)	-14.333	-7.916	Ascension Island
WIND00NAM	17.089	-22.575	Namibia
ZAMB00ZMB	28.31	-15.43	Zambia
SUTH00ZAF	20.810	-32.380	South Africa
JCTW00ZAF	18.469	-33.951	South Africa

Table 3.1: List of selected GNSS stations with their geographical coordinates and locations.

3.2 Methodology of our study

In this study, dual-frequency GNSS observations with a sampling rate of 120 measurements per hour were utilized to estimate TEC. The raw GNSS data were converted into Compact Measurement (CMN) files containing TEC values using the GPS-TEC Analysis software developed by Dr. Gopi (Seemala 2023). The conversion algorithm, based on dual-frequency carrier phase and pseudorange measurements, is described in Section 2.4. This approach enables reliable extraction of ionospheric electron density variations from GNSS signals.

To establish a reference for quiet ionospheric conditions, five geomagnetically quiet days prior to the storm were selected, excluding the day immediately preceding the event to avoid pre storm disturbances. These datasets were merged, and a time only column was generated to remove date dependency. TEC values were then averaged over five days and satellite PRNs for each time epoch, resulting in a representative quiet time TEC profile. For storm time analysis, data from three days before, two storm days, and three days after the event were combined into an eight day dataset .The quiet time average TEC profile was then combined with the eight day storm dataset. This enabled a direct comparison of TEC variation with time during quiet conditions, and TEC response during geomagnetic storm conditions.The results are presented as time series plots, with time on the x-axis, and TEC on Y-axis allowing clear visualization of

ionospheric perturbations across different phases of the storm.
All data processing, analysis, and visualization tasks were carried out using Python, leveraging several key scientific libraries. Pandas for data handling and time-series manipulation. NumPy for numerical computations and array operations. Matplotlib for data visualization. Matplotlib.dates for handling and formatting time-series data. These tools enabled efficient processing of large GNSS datasets, precise time alignment, and high-quality visualization of TEC variations.

3.3 EISCAT Analysis for Ion and Electron Temperature

The European Incoherent Scatter Scientific Association (EISCAT) operates a network of advanced incoherent scatter radars dedicated to investigating the Earth's ionosphere and upper atmosphere. Among its key facilities, the EISCAT Svalbard Radar (ESR), located in Svalbard (78.09°N, 16.01°E), is specifically designed for studying the polar ionosphere. In addition, the EISCAT UHF radar, situated in Tromsø (69.35°N, 19.14°E), operates at ultra-high frequencies and provides precise measurements of key plasma parameters, including ion temperature (T_i) and electron temperature (T_e). Together, these radar systems offer valuable insights into ionospheric dynamics, particularly during geomagnetic storms and other space weather events. EISCAT Level 3 data products can be directly accessed and downloaded from the official data portal (portal.eiscat.se), where datasets are provided in the HDF5 (Hierarchical Data Format). To efficiently handle and analyze these datasets, we employ the geospacelab Python library,this library supports multiple datasets, including EISCAT, GUVI, and OMNI, and provides a user-friendly interface for processing large volumes of ionospheric measurements and generating scientifically meaningful visualizations.

3.4 TIMED/GUVI and O/N_2 Ratio

The Thermosphere Ionosphere Mesosphere Energetics and Dynamics (TIMED) satellite is designed to study the energetics and composition of the Earth's upper atmosphere. One of its key instruments, the Global Ultraviolet Imager (GUVI), measures far ultraviolet emissions to derive important ionospheric and thermospheric parameters. Among these, the O/N_2 ratio represents the relative abundance of atomic oxygen to molecular nitrogen, serving as a crucial indicator of ionospheric composition. Variations in the O/N_2 ratio, particularly during geomagnetic storms, significantly influence ion-neutral chemistry and recombination rates, thereby affecting plasma density in the ionosphere.The GUVI L3 data are available at its official website (guvitimed.jhuapl.edu).

3.5 Geomagnetic Storm Parameters

The SYM-H index, obtained from the World Data Center for Geomagnetism, Kyoto, is a high-resolution 1-minute measure of the symmetric ring current intensity and is widely used to characterize geomagnetic storm evolution. The auroral electrojet indices (AE, AL, and AU), also provided by the same data center, represent the strength and variability of auroral currents, reflecting energy input into the high-latitude ionosphere. In addition to ground-based indices, key solar wind parameters such as proton density, solar wind velocity, and the interplanetary magnetic field (IMF) are obtained from the OMNI dataset. These parameters describe upstream solar wind conditions that drive geomagnetic activity through solar wind magnetosphere coupling. Together, these datasets provide a comprehensive framework for understanding solar wind drivers and magnetospheric response during geomagnetic storms.

Data availability

We have collecting data for SYM-H index ,Auroral upper,AL and AE from (https://wdc.kugi.kyoto-u.ac.jp/aeasy/index.html) and data for KP index from (https://kp.gfz-potsdam.de/en/data) and data for IMF,Solar Wind Speed,proton density and particle pressure from(https://omniweb.gsfc.nasa.gov/form/dx1.html). For GNSS data we have used (https://ga-gnss-data-rinex-v1.s3.amazonaws.com/index.html). (EISCAT SR) and EISCAT UHF level three data are avilable at (https://portal.eiscat.se/).TIMED GUVI level 3 processed data ,for O/N_2 ratio is available at (https://guvitimed.jhuapl.edu/).IRI model simulation is availabe at NASA's website (https://kauai.ccmc.gsfc.nasa.gov/instantrun/iri/).

CHAPTER 4

Results and Discussion

4.1 Comparative Analysis of Geomagnetic Storm Parameters

A detailed comparative analysis of geomagnetic storm parameters is presented for three major events: 10-11 May 2024 level G5, 10-11 October 2024 level G3, and 12-13 November 2025 level G2. The figure 4.1 illustrates key storm-time variations using SYM-H index, Kp index, auroral electrojet indices, solar wind speed, and proton density. Where SYM-H shows the strength of the ring current during storms, Kp gives the overall global disturbance level of the magnetic field, and AE indicates how active the auroral region was.These parameters collectively describe the intensity, evolution, and driving mechanisms of geomagnetic storms across different phases. Panels (a-c) represent the geomagnetic storm of 10-11 May 2024. In panel (a) the Kp index reaches a maximum value of 8.7 around 00:10 UT on 11 May, while the minimum SYM-H -518 value is observed a few hours later at approximately 02:10 UT on 11 May, indicating the main phase of the storm. In panel (b) solar wind speed exhibits a continuous increase from 16:36 UT on 10 May until 01:30 UT on 12 May, followed by a gradual decline. Proton density increases from 14:21 UT to 19:12 UT on 10 May, after which multiple fluctuations are observed before returning to near-normal levels at 16:25 UT on 11 May. Panel (c) shows strong variability in auroral electrojet activity, with maximum disturbance occurring around 16:55 UT on 10 May 2024. Panels (d-f) describe the 10-11 October 2024 storm, where the minimum SYM-H is recorded at 23:22 UT on 10 October and the maximum Kp occurs at 21:44 UT on the same day. In panel (e) a sharp increase in solar wind speed is observed around 12:55 UT on 10 October, followed by a gradual decrease, while proton density shows a sudden enhancement near 12:50 UT on 10 October, with multiple peaks before declining.Panel (f) highlights intense auroral activity, with AE reaching nearly 4500 nT around 16:21 UT on 10 October.

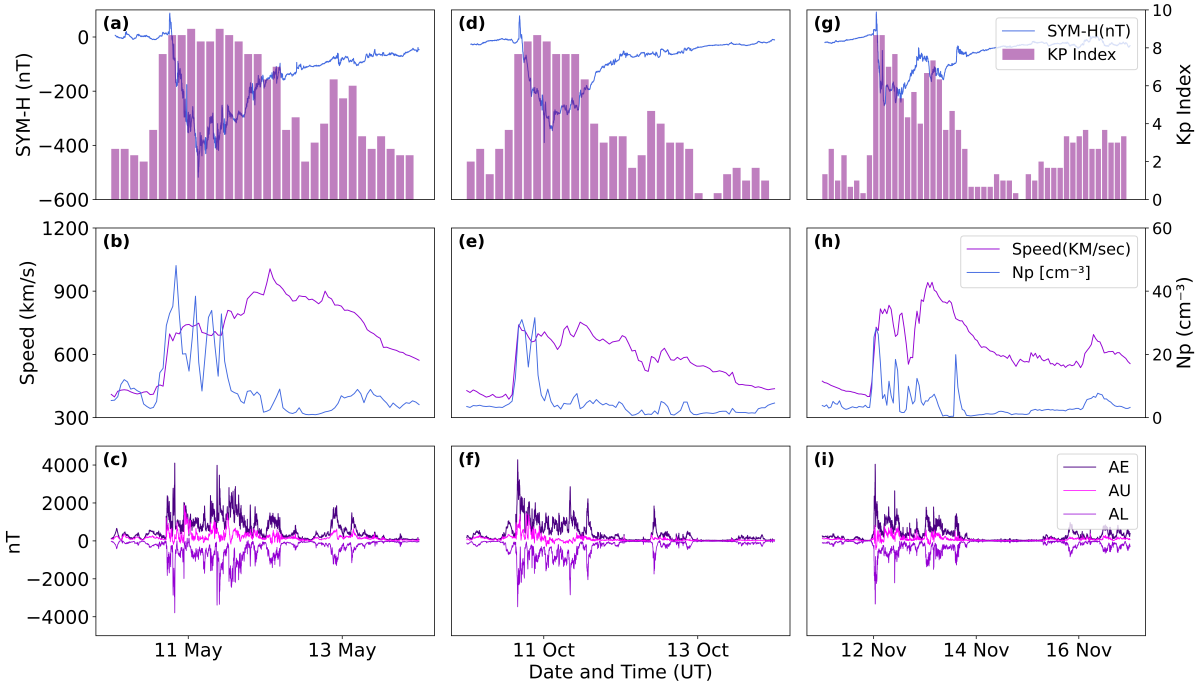

Figure 4.1: Important parameters of the magnetic storm,where panel (a-c) describes important magnetic storm parameter from 10-11 may 2024 magnetic storm.Panel (d-f) explain important storm parameter from magnetic storm 10-11 october 2024 and the panel (g-i) represent storm parameter from magnetic storm 12-13 november 2025. Figure (a,d,g) represent SYM-H index and KP index,Panel (b,e,h) solar wind speed and proton density variation,figure(c,f,i) represent Auroral variation.

Panels (g-i) correspond to the geomagnetic storm of 12-13 November 2025. In panel (g), the minimum SYM-H value occurs at approximately 04:12 UT on 12 November, indicating that the storm main phase develops during the dawn sector, with the maximum Kp value observed nearly simultaneously at 04:01 UT. In panel (h), solar wind speed begins to increase from 00:45 UT on 12 November, exhibits a temporary dip near 16:45 UT on the same day, and subsequently rises again to a peak value of about 935 km s^{-1} at 01:12 UT on 13 November before gradually decreasing. Proton density reaches its maximum around 01:12 UT on 12 November 2025, displaying multiple peaks, and eventually returns to normal levels by approximately 19:45 UT on 13 November. Panel (i) shows strong auroral activity, with the AE index peaking at approximately 4100 nT around 00:30 UT on 12 November 2025. The onset, peak intensity, and recovery phases of all three geomagnetic storms are further summarized systematically in Table 4.1.

Name of Geomagnetic Storm	Date of Geomagnetic Storm	Strength	Beginning of storm and recovery phase
Mother's Day Super Storm	10–11 May (2024)	-518	(10 May 17:55 UT)–(11 May 2:15 UT)
October 2024 Superstorm	10–11 October (2024)	-335	(10 Oct 15:14 UT)–(11 Oct 1:00 UT)
November 12-13 (2025)	November 12-13 (2025)	-254	(12 November 00:10 UT)–(12 November 03:52 UT)

Table 4.1: Major geomagnetic storms, their onset and beginning of the recovery phase .

The pronounced variations observed in the SYM-H index, auroral electrojet currents, solar wind speed, and proton density provide clear evidence of enhanced solar wind-magnetosphere coupling associated with geomagnetic storm activity. Among the events analyzed, the 10-11 May 2024 storm stands out as the most intense (Lee et al. 2025), classified as a G5 (extreme) event, characterized by strong ring current development and significant energy input into the magnetosphere. This is followed by the 10-11 October 2024 storm, categorized as a G3 (strong) event, and the most recent 12-13 November 2025 storm, identified as a G2 (moderate) event. These variations collectively highlight the differing intensities.

4.2 TEC profile of three geomagnetic stroms

4.2.1 Ionospheric Response to the 10-11 May 2024 Geomagnetic Storm

The 10-11 May 2024 geomagnetic storm represents one of the most intense space weather event, producing significant disturbances in radio communication and satellite-based systems (Kivelson and Russell 1995).In this section, we analyze the ionospheric response using multi station GNSS observations to understand latitude-dependent behavior during this storm.

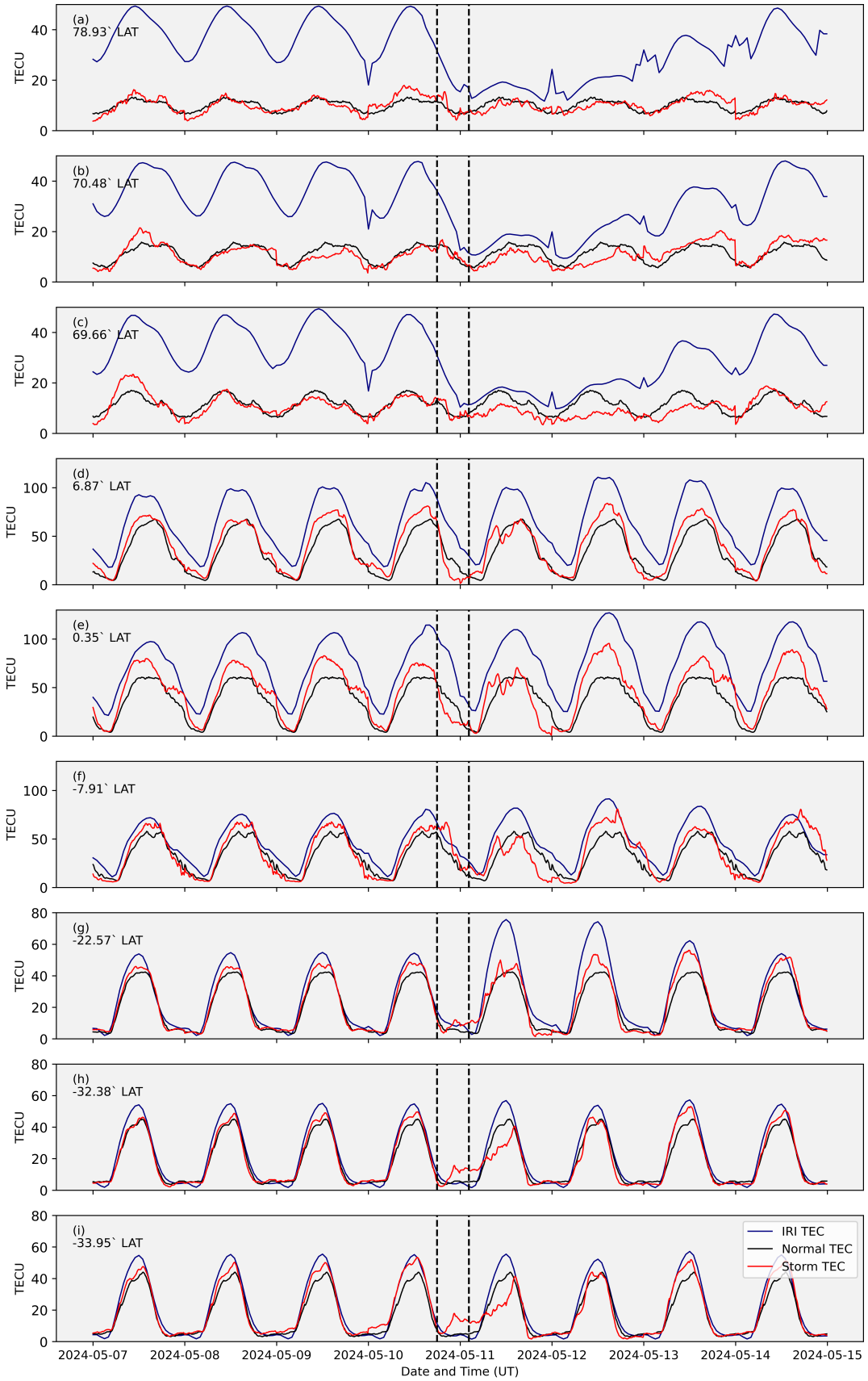

Figure 4.2: This figure represent TECU variation on May 2024 magnetic storm at all the nine GNSS stations,panel (a-c) represent High latitude region,panel (d-f) represent equatorial region, and from (g-i) represent mid-Latitude.Beginning of the magnetic storm and the start of recovery phase is represented by black dotted line.Black curve represent the average storm day and Blue line represent IRI TEC prediction and red curve represent storm time TEC.

Figure 4.2 presents time-series variations of TEC for nine GNSS stations, covering three days prior to the storm, two storm days (10-11 May 2024), and three days after the event. The stations are distributed across polar, equatorial and mid-latitude regions along approximately the 0° meridian, and their details are provided in Table 3.1. A five-day quiet-time average TEC is shown as a reference (black curve), while storm-time TEC is represented in red. Panels (a-c) correspond to high-latitude stations. In panel (a), representing NYA100NOR (78.93°N), located near the polar cap region, nighttime TEC on 10 May shows minimal variation during storm commencement; however, on 11 May, TEC values remain slightly lower than the quiet-time reference (Cai et al. 2026). In panel (b), corresponding to SCOR00GRL (70.48°N) near the auroral region, TEC on 11 May remains consistently lower by approximately 2-3 TECU compared to the average curve. Similarly, panel (c), representing TRO100NOR (69.663°N), also within the auroral zone, shows a clear depletion in TEC, with storm-time values 10-11 TECU significantly lower than the quiet-time by 15 TECU, indicating pronounced ionospheric depletion across the polar region during the storm.

Panels (d-f) represent equatorial stations. In panel (d) (6.87° latitude), TEC during 10-11 May shows a noticeable reduction compared to both pre-storm and post-storm days as well as the quiet-time reference. Panel (e) (0.354° latitude) exhibits a similar trend, although with slightly enhanced variability relative to panel (d). In panel (f) (−7.916° latitude), which appears more sensitive among the equatorial stations, TEC values during the storm period are consistently higher than both surrounding days and the average reference curve,after the the storm day on 11 may ,a unusual dip is noticed during the peak time (Pal et al. 2025). Panels (g-i) correspond to mid-latitude stations in the Southern Hemisphere. In panel (g) (−22.57° latitude), an increase in TEC is observed during the storm onset on 10 May, and elevated TEC persists into 11 May compared to the reference curve. However, in panels (h) (−32.38° latitude) and (i) (−33.95° latitude), TEC initially increases during storm onset but decreases on 11 May relative to the quiet-time level. Overall, the results indicate a complex latitudinal response, with consistent depletion in polar regions, while mid-latitudes and equatorial exhibit mixed behavior with both enhancement and depletion depending on location and storm phase.Where as the International Reference Ionosphere (IRI) which is an empirical model that provides a standard representation of ionospheric parameters such as molecular composition,ion temperature,TECU etc,based on long-term observations from ground-based and satellite measurements,performs very well in the high latitude region clearly showing TECU depletion in all three stations.In the equitorial region no significant variation can be noticed on all the three stations,compare to there pre and post storm days.Where as in the mid latitude region ,the IRI model clearly shows the peak at (−22.57° latitude),and no variation on other two station,overall the IRI model performes very well.

4.2.2 Ionospheric Response to the 10-11 October 2024 Geomagnetic Storm

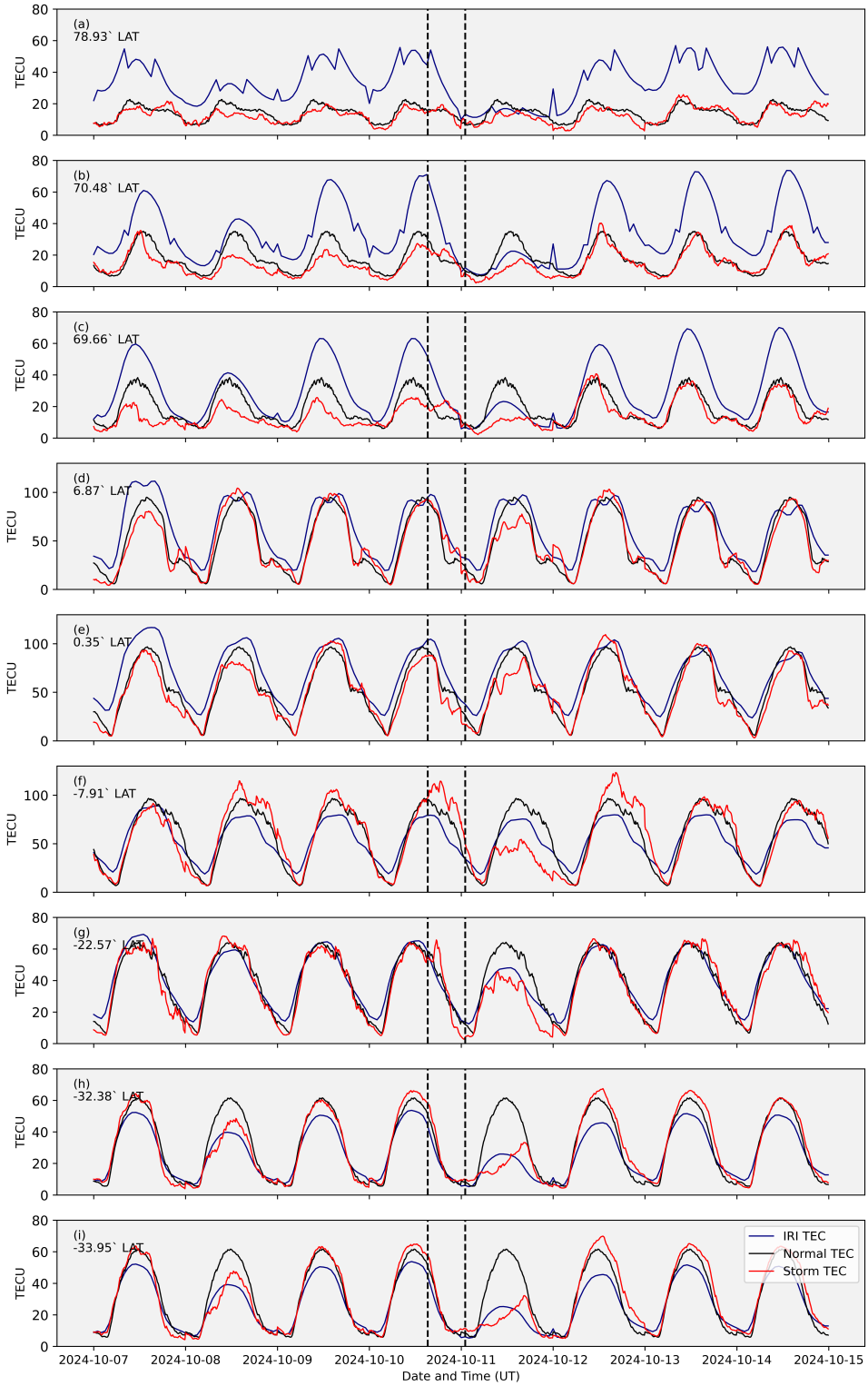

Figure 4.3: This figure represent TECU variation on October 2024 magnetic storm at all the nine GNSS stations,panel (a-c) represent High latitude region,panel (d-f) represent equatorial region, and from (g-i) represent mid-Latitude.Beginning of the magnetic storm and the start of recovery phase is represented by black dotted line.Black curve represent the average storm day and Blue line represent IRI TEC prediction and red curve represent storm time TEC.

The ionospheric response to the 10-11 October 2024 geomagnetic storm, classified as a G3 (strong) event, is analyzed using multi station GNSS TEC observations. The SYM-H index reached a minimum value of approximately −335 nT, indicating a significant enhancement of the ring current. The storm commenced at 15:14 UT on 10 October 2024, while the recovery phase began at approximately 01:00 UT on 11 October 2024 (figure 4.1). Figure 4.3 presents the time-series variation of TEC from 7 October to 14 October 2024, allowing comparison between pre-storm, storm-time, and post-storm conditions. Panels (a-c) represent high-latitude stations in the Northern Hemisphere. Panel (a), corresponding to the GNSS station NYA100NOR (78.93° latitude) located near the polar cap region, shows a clear depletion in TEC on 11 October, where storm-time values fall noticeably below the quiet-time reference curve. Similarly, panel (b), representing SCOR00GRL (70.48° latitude) near the auroral region, exhibits a significant reduction in TEC throughout 11 October, indicating strong ionospheric depletion associated with enhanced geomagnetic activity. In panel (c), corresponding to TRO100NOR (69.663° latitude), also within the auroral zone, a pronounced decrease is observed, where TEC drops to approximately 12 TECU around 14:10 UT on 11 October, compared to a quiet-time reference value of nearly 35 TECU, indicating an approximate 66% reduction. These observations collectively confirm strong plasma depletion in the polar and auroral regions during the storm main phase.

Panels (d-f) represent equatorial stations, where a consistent decreasing trend in TEC is observed across all locations on 11 October. Around 14:15 UT on 11 October, a noticeable reduction of approximately 20-30% is evident in all equatorial stations relative to their respective quiet-time reference levels (Paul et al. 2025), indicating suppression of equatorial ionization during the disturbed conditions. In contrast, the mid-latitude stations in the Southern Hemisphere exhibit a more complex response. At the GNSS station located at −15.4° latitude (panel g), an increase in TEC is observed during the storm onset time followed by a continuous decrease started from recovery phase and remains till the next day . However, in panel (h), corresponding to the station at approximately −32° latitude, a clear decrease in TEC is observed, indicating storm-time depletion. A similar decreasing trend is also evident in panel (i), corresponding to the GNSS station at approximately −34° latitude, where TEC variations closely follow the behavior observed at −32° latitude. Therefore, the overall response indicates a consistent decrease in TEC across the polar regions during the 10–11 October 2024 geomagnetic storm, while mid-latitude and equatorial regions exhibit mixed behavior, with localized enhancement during the onset of the storm and depletion at 11 october, reflecting the combined effects of composition changes and electrodynamic plasma transport.The IRI model prediction of october magnetic storm are very interesting , where in the high latitude region depletion in TECU is predicted in all the region. The model prediction in the equatorial region show no variation, in any of the

station compare to pre and post days of 11 october which recovery phase magnetic storm.In the mid latitude region at $-22.57°$ lat slight depletion is predicted on 11 october, at $-34°$ and $-32°$ significant depletion is predicted compare to $-22.57°$.As a result we can conclude that the IRI model predictes well at high latitudes and mid latitudes but it unable to predict the depletion at TECU on 11 october on equatorial region.

4.2.3 Ionospheric Response to the November 2025 Geomagnetic Storm

The November magnetic storm is the most recent storm in our study it is G2 level moderate storm . With SYM-h index value reaches to -254 nT and the magnetic storm begins at 00:10 ut 12 November . Figure 4.4 presents the corresponding time-series variations. In panel (a), corresponding to the GNSS station located near the polar cap region, a pronounced enhancement in TEC is observed, with a clear spike occurring at 13:55 UT on 12 November, where the TEC reaches nearly 15 TECU, compared to a quiet-time reference value of approximately 6-7 TECU, indicating nearly a twofold increase. In panel (b), representing a high-latitude GNSS station near the auroral oval, a sustained increase in TEC is observed from the beginning of the storm, with the storm-time TEC approaching the reference curve around 14:15 UT on 12 November. Similarly, in panel (c), another auroral-region station shows a clear enhancement, where at 11:44 UT on 12 November, the TEC reaches approximately 17 TECU, compared to a reference value of about 15 TECU, confirming a positive ionospheric response in the high-latitude region.

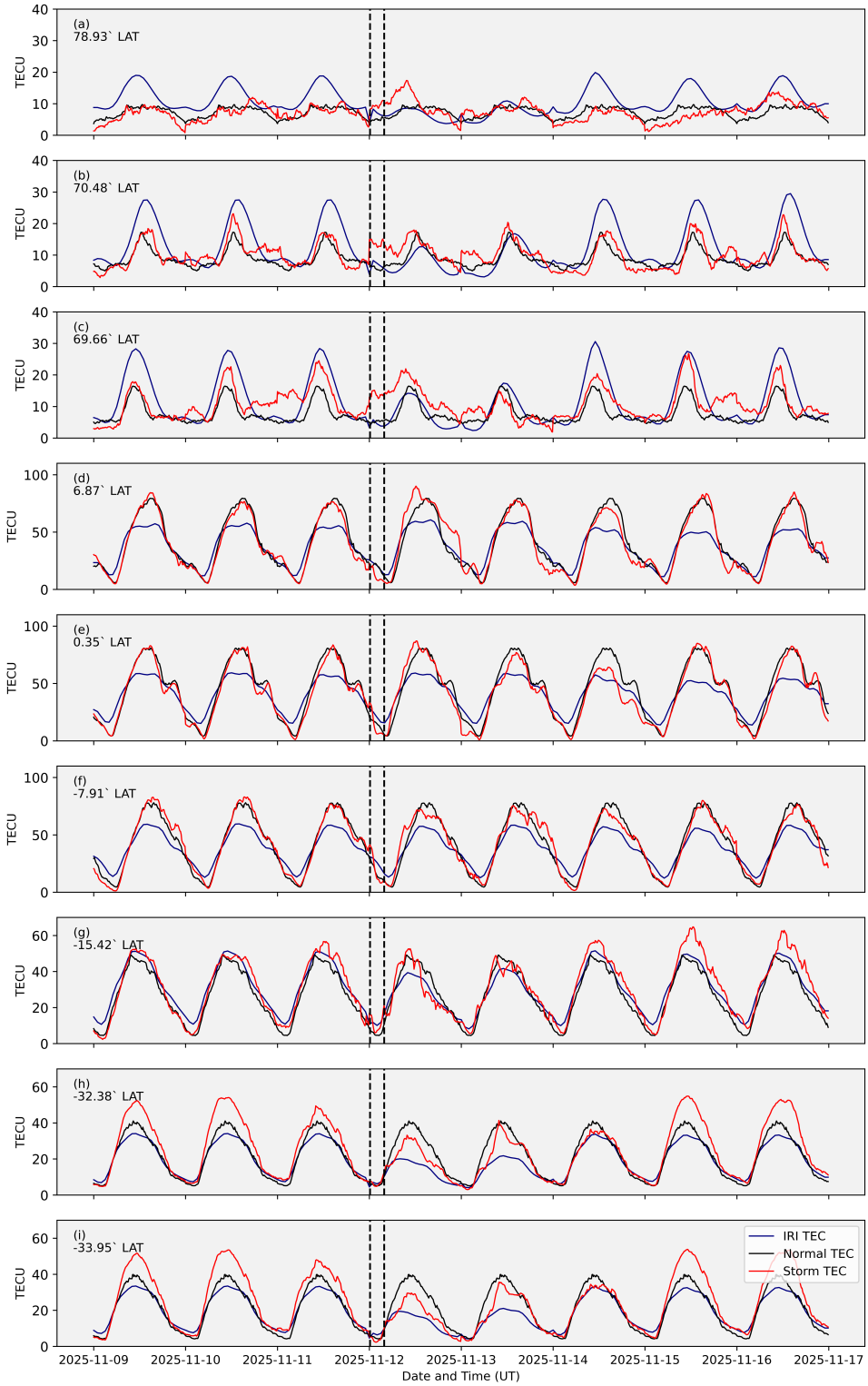

Figure 4.4: This figure represent TECU variation on November 2025 magnetic storm at all the nine GNSS stations, panel (a-c) represent High latitude region, panel (d-f) represent equatorial region, and from (g-i) represent mid-Latitude. Beginning of the magnetic storm and the start of recovery phase is represented by black dotted line.Black curve represent the average storm day and Blue line represent IRI TEC prediction and red curve represent storm time TEC.

Panels (d-f) represent the equatorial region, where little bit of enhancement is noticed during the noon time of 12 november. In panel (d), corresponding to the station at 6.87° latitude,

a clear storm-time enhancement is observed around 11:55 UT on 12 November 2025. In panel (e), near 0.354° latitude, the TEC reaches approximately 85 TECU at 11:53 UT on 12 November, compared to a quiet-time value of about 80 TECU, indicating an increase of nearly 6%. However, in panel (f), a slight decrease of approximately 2-3% is observed at noon time 12 november, suggesting localized variability within the equatorial region. In the mid-latitude region (panels g-i), a mixed response is observed. In panel (g), corresponding to the station at $-15.4°$ latitude, a slight enhancement in TEC is observed near the daytime peak. In contrast, panels (h) and (i), corresponding to stations at higher mid-latitudes, exhibit a decrease in TEC after the recovery phase, where storm-time values drop to approximately 36 TECU compared to the reference value of about 40 TECU, indicating nearly a 12% reduction. Overall, these observations suggest that the November 2025 geomagnetic storm exhibits characteristics of a positive ionospheric storm, with enhanced TEC in the polar and equatorial regions.The IRI model fails to accurately reproduce the TEC enhancement observed at all three polar GNSS stations on 12 November. In contrast, in the equatorial region, the model predicts a relatively steady TEC behavior that is consistent with our observations. Similarly, at the mid-latitude station ($-22.57°$), the model captures a stable TEC variation in agreement with our obsevation. Furthermore, at higher mid-latitudes ($-32°$ and $-34°$), the model predicts a depletion in TEC during the storm period relative to pre- and post-storm conditions, which is also consistent with our observations.

4.3 Ion Temperature (T_i) and Electron Temperature (T_e) profile of three geomagnetic storms

4.3.1 Analysis of Ion Temperature (T_i) and Electron Temperature (T_e) May 2024 magnetic Storm

In this study, ionospheric thermal variations are investigated using measurements of ion temperature (T_i) and electron temperature (T_e) obtained from the EISCAT radar systems. Specifically, data from the EISCAT Svalbard Radar (ESR; 78.09°N, 16.01°E) and the EISCAT UHF radar located in Tromsø (69.35°N, 19.14°E) are utilized to examine temperature variations across three different days. The European Incoherent Scatter Scientific Association (EISCAT) operates these advanced radar systems to provide detailed diagnostics of ionospheric plasma parameters. In the presented figure **??**, panel (p) illustrates the variation of T_i and T_e on 10 May 2024 from 13:00 ut to 23:59 ut, panel (q) represents the corresponding variations on 11 May 2024 during the peak phase of the geomagnetic storm, and panel (r) shows observations from the EISCAT UHF radar on 12 May 2024 for full day, which is considered a quiet-time reference day for comparison.

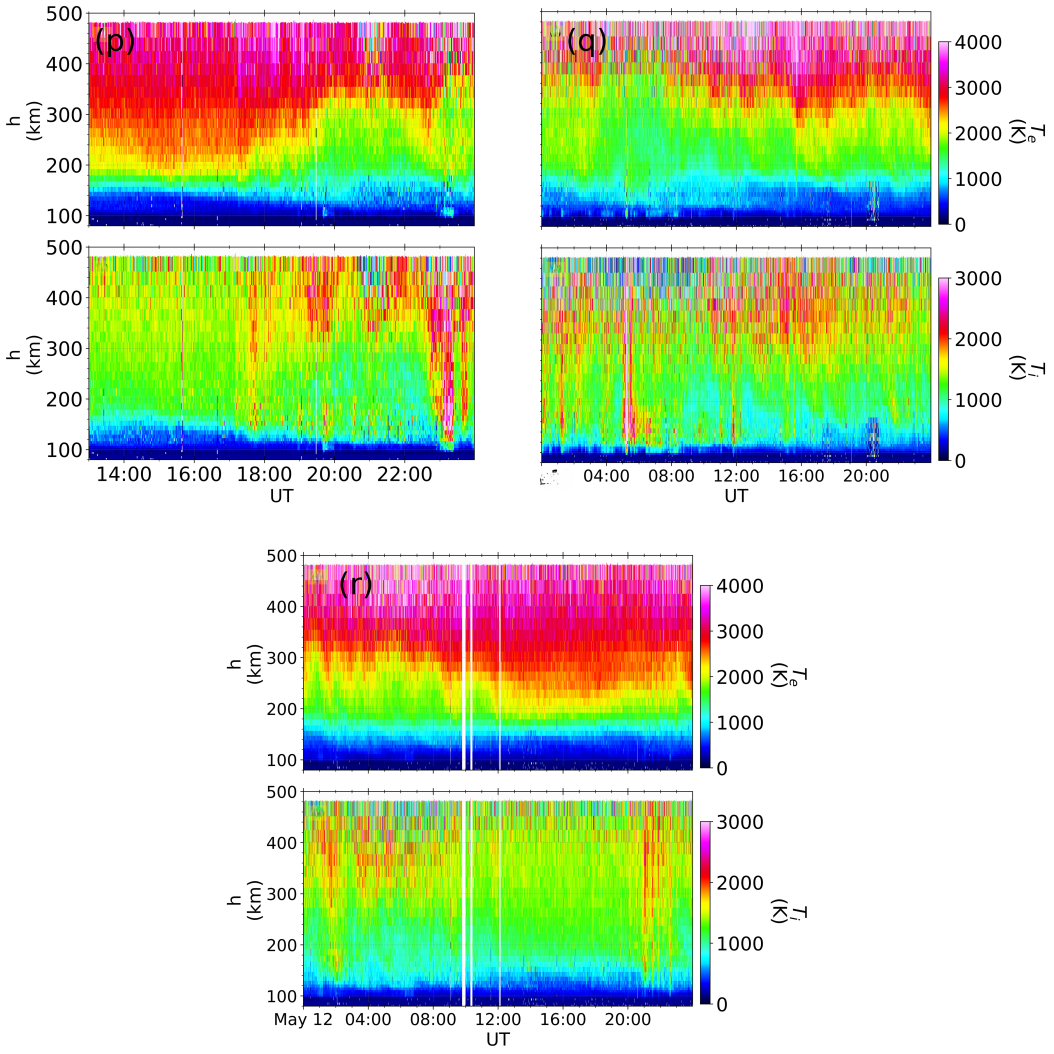

Figure 4.5: This figure represent time series plot of T_i and T_e , figure (p) represent temperature variation on day 10 May, (q) represent variation for temperature on the day 11 may and (r) represent temperature variation on 12 may

From the analysis, a significant enhancement in both ion temperature (T_i) and electron temperature (T_e) is clearly observed during the disturbed days of 10-11 May 2024 compared to the relatively stable conditions on 12 May 2024. The increase in T_e and T_i is indicative of enhanced energy input into the ionosphere through mechanisms such as particle precipitation and Joule heating during geomagnetic activity. These elevated temperatures play a crucial role in modulating ionospheric chemistry, as both ion-neutral reaction rates and charge exchange processes are strongly temperature dependent. Consequently, higher T_i and T_e lead to increased recombination rates (Killeen et al. 1984), which contribute to the observed depletion in electron density and TEC during the storm period.

4.3.2 Analysis of Ion Temperature (T_i) and Electron Temperature (T_e) for the October 2024 Geomagnetic Storm

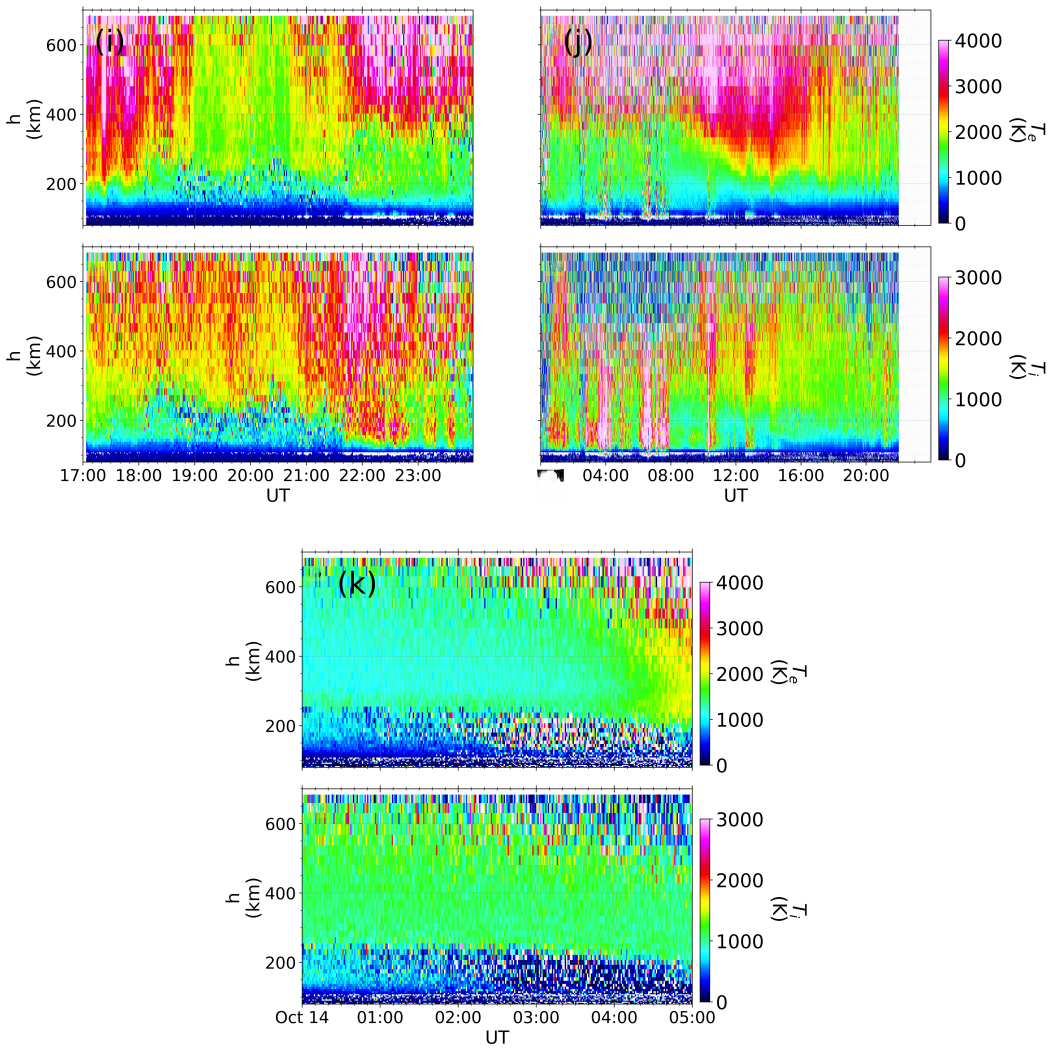

Figure 4.6: This figure represent time series plot of T_i and T_e ,figure (i) represent temperature variation on day 10 October,(j) represent variation for temperature on the day 11 October and (k) represent temperature variation on 14 October.

The ionospheric thermal response during the October 2024 geomagnetic storm is examined using ion temperature (T_i) and electron temperature (T_e) measurements obtained from the EISCAT Svalbard Radar (ESR) and the EISCAT UHF radar, focusing on high-latitude temporal variations. Figure 4.6 presents three panels (i-k), each corresponding to different observation periods: panel (i) represents data for 10 October 2024, with measurements available from 17:00 UT to 23:59 UT; panel (j) corresponds to 11 October 2024, where continuous observations are available for the full 24-hour period; and panel (k) represents 14 October 2024, with data available from 00:00 UT to 05:00 UT, which is considered a quiet-time reference. A clear and significant enhancement in both T_i and T_e is observed during the storm days (10-11 October) in

comparison to the quiet day (14 October). Specifically, the average temperature on 14 October is approximately 1100 K for both T_i and T_e, whereas during the storm period on 10-11 October, the average temperature increases to nearly 2250 K, with a pronounced peak observed around 14:10 UT on 11 October, indicating nearly a twofold increase. Elevated temperatures significantly influence ionospheric chemistry, as higher T_i and T_e enhance the rates of ion-neutral and charge exchange reactions (Killeen et al. 1984).

4.3.3 Ion Temperature (T_i) and Electron Temperature (T_e) Profile of the November 2025 Geomagnetic Storm

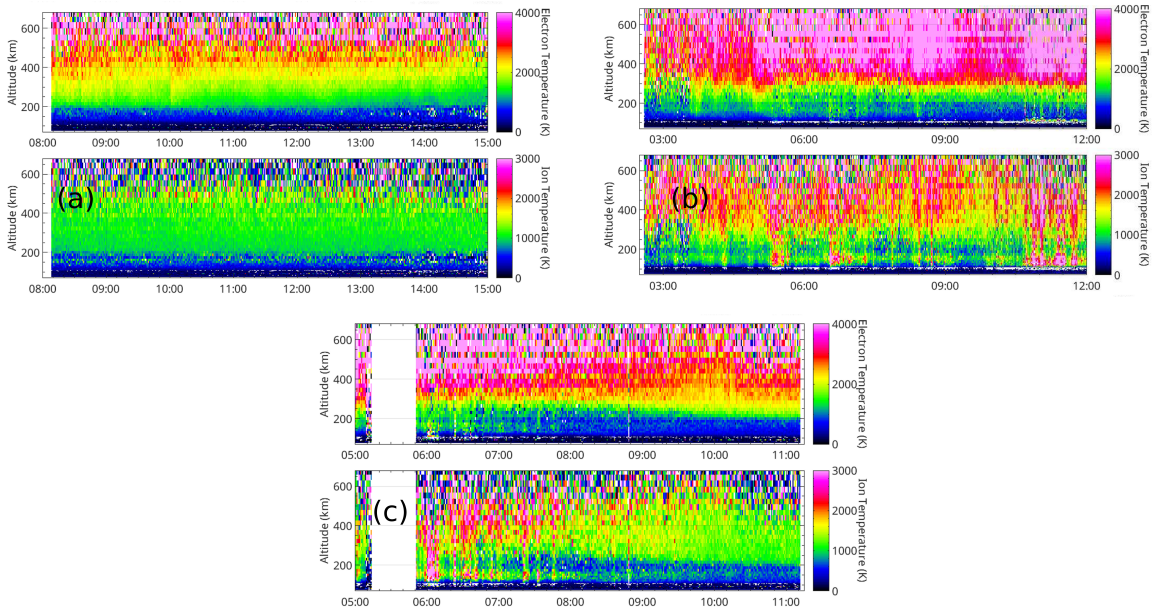

Figure 4.7: This figure represent time series plot of T_i and T_e ,figure (a) represent temperature variation on day 11 November,(b) represent variation for temperature on the day 12 November and (c) represent temperature variation on 13 November(Credit :https://portal.eiscat.se/)

Measurements obtained from the (ESR) and EISCAT UHF radar systems are interpreted in this section. Figure 4.7 presents the variation of T_i and T_e across three panels: panel (a) corresponds to 11 November 2025, where observations are available from 08:00 UT to 15:00 UT and represent relatively quiet conditions; panel (b) corresponds to 12 November 2025, with measurements from 02:30 UT to 12:00 UT, capturing the storm-time response; and panel (c) represents 13 November 2025, with data available from 05:00 UT to 11:00 UT, also within the disturbed period. A clear and significant enhancement in both T_i and T_e is observed on 12-13 November compared to 11 November. Specifically, the average electron temperature above 300 km altitude on 12 November is approximately 3800 K, while on 13 November it remains elevated at around 3100 K, The increase in ion and electron temperatures during the November 2025 geomagnetic storm exceeds that observed during the May and October 2024

events. Furthermore, as observed in Figure 4.4, TEC values during November remain relatively higher in the high-latitude region compared to the May and October events, suggesting increased plasma availability. This enhanced plasma density leads to more frequent collisions between charged and neutral particles, thereby intensifying Joule heating and contributing to the elevated T_i and T_e observed during the November storm.

4.4 Ionospheric Composition Analysis of two different geomagnetic storm

4.4.1 Ionospheric Composition Analysis Using GUVI O/N_2 Ratio of May 2024 magnetic storm

The ionospheric composition during the May 2024 geomagnetic storm is analyzed using the O/N_2 ratio derived from the Global Ultraviolet Imager (GUVI) onboard the Thermosphere Ionosphere Mesosphere Energetics and Dynamics (TIMED) satellite. This parameter plays a crucial role in controlling ionospheric electron density through ion-neutral chemistry. In this section, we examine the temporal and spatial evolution of the O/N_2 ratio to understand compositional changes associated with geomagnetic disturbances.

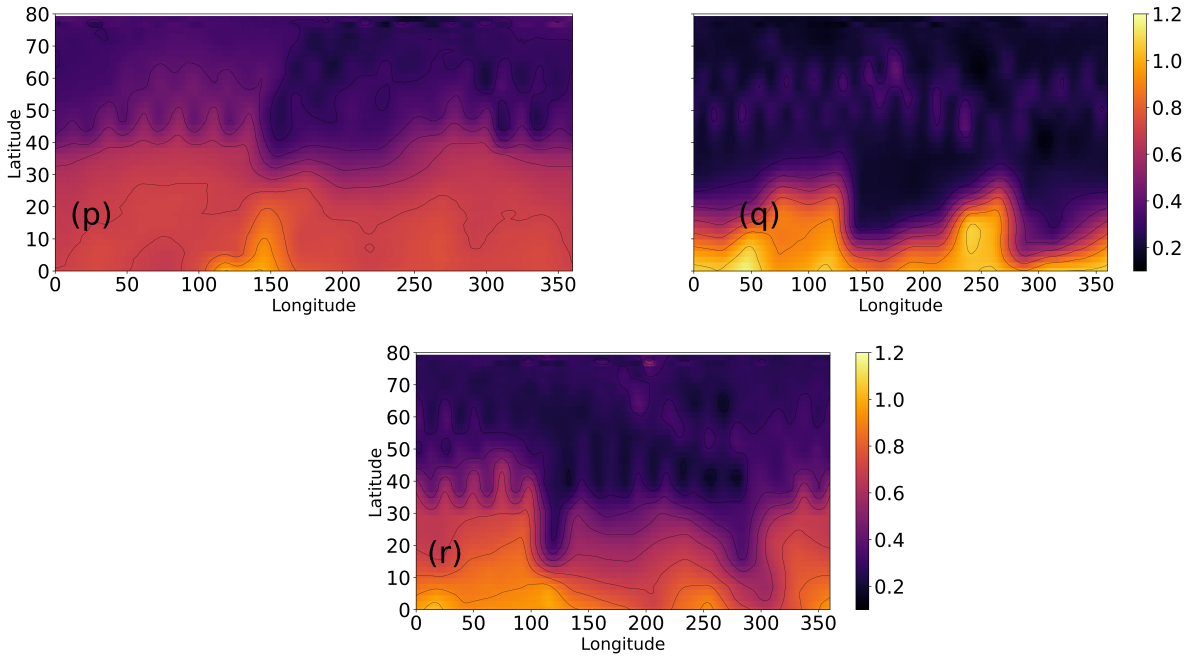

Figure 4.8: GUVI data represent latitude longitude variation of O/N_2 ratio, figure (p) represent 10 May, figure (q) represent 11 may, and 12 May is represented by figure (r).

Figure 4.8 presents the global distribution of O/N_2 ratio for three consecutive days, with panel (p) representing 10 May, panel (q) representing 11 May, and panel (r) representing 12 May 2024. A clear and systematic decrease in the O/N_2 ratio is observed from 10-12 May to 11 May, indicating significant compositional changes during the storm period. Considering the 0° meridian, in the polar latitude region (66°–80°), the O/N_2 ratio decreases from approximately 0.31 on 10 May to about 0.17 on 11 May, corresponding to nearly a 45% reduction. Similarly, in the mid-latitude region (20°-35°), the ratio shows a pronounced decrease from around 0.7 on 10 May to approximately 0.2 on 11 May, representing nearly a 70% reduction. In contrast, the equatorial region does not exhibit a significant decrease in O/N_2 ratio, indicating relatively weaker compositional disturbance. This overall decrease in O/N_2 ratio suggests an enhancement in molecular species such as N_2, which leads to increased recombination rates (Heelis and Hanson 1998).

4.4.2 Ionospheric Composition Analysis of the October 2024 magnetic storm

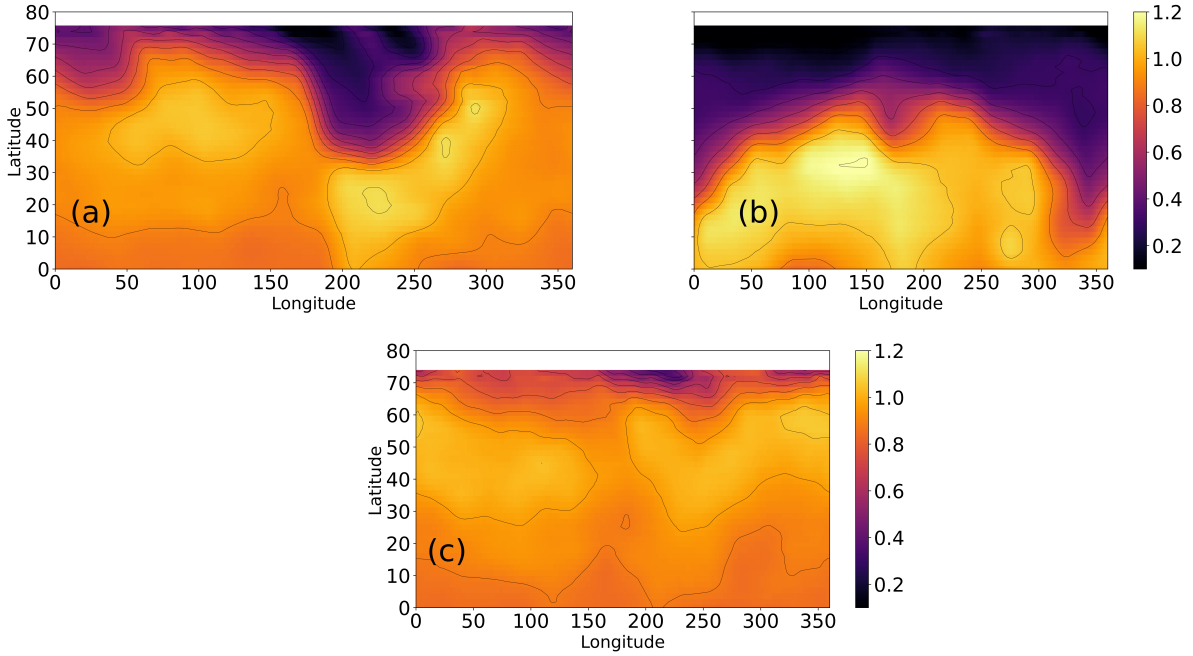

Figure 4.9: GUVI data represent latitude longitude variation of O/N_2 ratio, figure (a) represent 10 October, figure (b) represent 11 October, and 14 October is represented by figure (c).

The ionospheric composition is analyzed on the three days of October , focusing on the temporal and spatial variation of the O/N_2 ratio. This parameter serves as a key indicator of thermospheric composition and plays a crucial role in controlling ionospheric chemistry. Figure 4.9 presents three global maps corresponding to panels (a to c), where panel (a) represents the O/N_2 distribution on 10 October 2024, panel (b) corresponds to 11 October 2024, and panel (c) represents 14 October 2024. These observations allow a detailed comparison of compositional changes during the progression of the geomagnetic storm.

Examining the variation along the 0° meridian, a clear and systematic decrease in the O/N_2 ratio is observed from 14 October to 11 October in the high-latitude region. Specifically, the O/N_2 value decreases from approximately 0.83 on 14 October to about 0.19 on 11 October, corresponding to nearly a 77% reduction. In contrast, the equatorial region shows relatively stable behavior, with O/N_2 remaining nearly constant at approximately 1.04 ± 10–12% across all three days, indicating minimal compositional disturbance. The most significant variation is observed in the mid-latitude region, where O/N_2 values remain around 0.92 on 10 and 14 October, but decrease sharply to approximately 0.38 on 11 October, representing nearly a 58% reduction. This pronounced decrease in the O/N_2 ratio indicates thermospheric upwelling and enhanced molecular composition (increase in N_2 and O_2), thereby creating favorable conditions for ion-neutral and charge exchange reactions.

4.5 Observed Electron Density from ESR

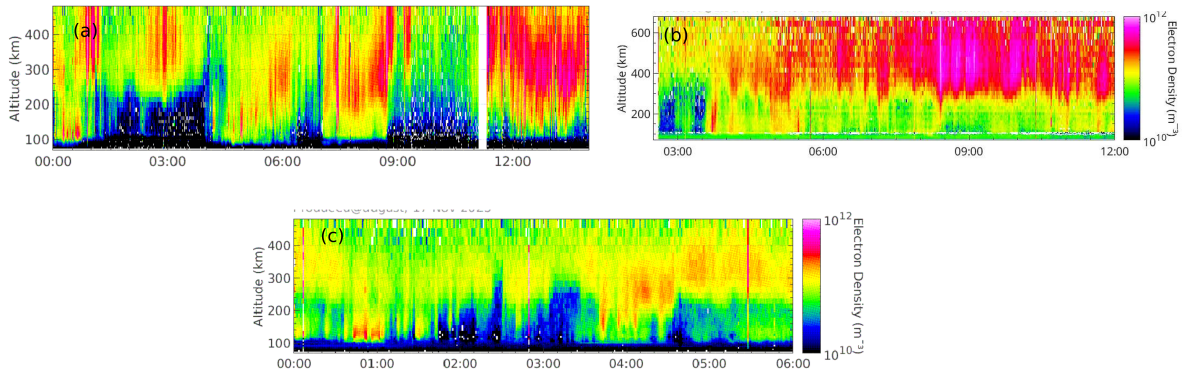

Figure 4.10: Electron density observation form the ESR,panel (a) represent 7 november (b) represent 12 november (c) represent observation from 14 November(Credit :https://portal.eiscat.se/).

In order to demonstrate the TEC enhancement in the high-latitude region during the 12 November geomagnetic storm, Figure 4.10 presents the electron density observed from ESR for three different days. Panel (a) represents observations for 7 November from 00:00 to 14:00 UT, panel (b) represents 12 November from 02:30 to 12:00 UT, and panel (c) represents 14 November from 00:00 to 06:00 UT. On 7 November, around 05:00 UT, the average electron density is approximately 8.5×10^{11} m^{-3}. On 14 November, at the same time, the average electron density is about 4.1×10^{11} m^{-3}, whereas on 12 November, around the same time, the electron density increases to approximately 2.4×10^{12} m^{-3}. Thus, a clear enhancement in electron density is observed on 12 November compared to both 7 and 14 November.

4.6 Interpretation of the Outcomes

May and October 2024 magnetic storm

The ionospheric response during the May and October 2024 geomagnetic storm clearly indicates a significant depletion in Total TEC across the high-latitude region. During this period, the enhanced influx of high-energy particles into the polar ionosphere leads to increased collisions with neutral species, resulting in substantial thermospheric heating and upwelling (Heelis and Hanson 1998). This process increases the concentration of molecular species such as N_2, thereby reducing the O/N_2 ratio and creating favorable conditions for ion-neutral and charge exchange reactions. The dominant reactions governing this process can be expressed as (St.-Maurice and Hanson 1982):

$$O^+ + N_2 \rightarrow NO^+ + N \tag{4.1}$$

$$O^+ + O_2 \rightarrow O_2^+ + O \tag{4.2}$$

The reaction rate coefficient for the primary ion-neutral interaction is given by (St.-Maurice and Hanson 1982):

$$k = \left[1.53 \times 10^{-12} - 5.92 \times 10^{-13} \left(\frac{T_{\text{eff}}}{300}\right) + 8.6 \times 10^{-14} \left(\frac{T_{\text{eff}}}{300}\right)^2\right] \text{cm}^3\,\text{s}^{-1}, \tag{4.3}$$

$$T_{\text{eff}} = 0.636\,T_i + 0.364\,T_e. \tag{4.4}$$

The enhanced production of molecular ions (NO^+ and O_2^+) leads to efficient dissociative recombination, which proceeds at a much faster rate than radiative recombination (Heelis and Hanson 1998), thereby causing a rapid reduction in electron density.

In the mid-latitude region ($-32.38°$ and $-33.95°$), although direct O/N_2 measurements are not available, insights can be inferred from corresponding northern hemisphere observations, which show a significant decrease in O/N_2 ratio during the geomagnetic storm. This compositional change implies enhanced molecular dominance, leading to increased recombination rates and consequent TEC depletion. The observed decrease in TEC at these latitudes during 10-11 May (Cai et al. 2026) and October 2024 is therefore consistent with storm-time thermospheric circulation and composition changes that propagate from high to mid-latitudes. Additionally, the increase in (T_i) and (T_e), as observed in earlier analysis, further enhances reaction rates, reinforcing the depletion mechanism.

In contrast, the equatorial region exhibits a different response due to the dominance of electrodynamic processes. It is well established that solar heating causes an upward expansion of the plasma layer, which is subsequently transported via the $\mathbf{E}\times\mathbf{B}$ drift mechanism (Keidar and Beilis 2006). This leads to plasma accumulation in the equatorial ionization anomaly (EIA) region, typically between $\pm15°$ to $\pm22°$ latitude. As a result, a redistribution of plasma occurs, causing a decrease in TEC near the equator and an enhancement in TEC at low- to mid-latitudes. This behavior explains the observed increase in TEC at one mid-latitude station around $-22.57°$ and decrease at others (Lee et al. 2025), highlighting the complex coupling between composition, chemistry, and electrodynamics during geomagnetic storm conditions.

November 2025 Magnetic Storm

The November 2025 geomagnetic storm can be characterized as a positive ionospheric storm, as an overall increase in TEC is observed in both the high-latitude and equatorial regions (Fuller-Rowell and Rees 1981).In the northern high-latitude region, from the beginning of October to the end of March, the polar cap experiences continuous darkness, resulting in

significantly reduced solar heating of the thermosphere. Consequently, thermospheric expansion is limited, and there is no substantial increase in molecular species such as N_2 and O_2 in the ionosphere(Unfortunately, O/N_2 ratio data for the November 2025 geomagnetic storm are not available) (Fuller-Rowell and Rees 1981). Under such conditions, recombination processes remain relatively slow due to the dominance of atomic oxygen. Therefore, when the geomagnetic storm commences at 00:12 UT on 12 November 2025, enhanced plasma influx into the polar region leads to an overall increase in electron density, as loss processes are not sufficiently strong to offset production and transport effects. In the equatorial region, the storm onset occurs during the dawn sector, when solar heating is still minimal and the equatorial fountain mechanism is not fully developed. As a result, the usual redistribution of plasma via the $\mathbf{E} \times \mathbf{B}$ drift is weak, allowing plasma to accumulate locally rather than being transported to higher latitudes. This leads to a direct increase in TEC in the equatorial region during the initial phase of the storm. Thus, the combined effects of reduced recombination in the polar night ionosphere and suppressed fountain dynamics at dawn contribute to the observed positive storm signature during the November 2025 event.

Summary

In this study, utilizing publicly available global GNSS data, we have systematically investigated the ionospheric response across three distinct latitude regions ,high latitude, mid-latitude, and low latitude during multiple geomagnetic storm events. These include the G5 level May 2024 magnetic storm, the G3 October 2024 magnetic storm, and the most recent G2 November 2025 moderate magnetic storm.

The analysis reveals that during the May and October storms, a consistent reduction in plasma density is observed across all latitude regions, except at $-22.57°$ during the may magnetic storm, where the TEC increases due to equatorial anomaly. Indicating the dominance of composition driven processes, particularly enhanced recombination associated with reduced O/N_2 ratios. The observed decrease in plasma density in the high-latitude region during the May storm is consistent with results reported in previous study employing different methodologies, thereby validating our findings (Cai et al. 2026).

In contrast, the November 2025 magnetic storm demonstrates the characteristics of a positive ionospheric storm, with a noticeable increase in TEC in both high-latitude and equatorial regions, suggesting a dominant influence of plasma transport and less heating due to complete darkness during November in north pole. The TEC enhancement at the high latitude region is verified from the observation of the EISCAT Svalbard Radar (ESR) section 4.5.

In this study, the molecular composition dependence of the ionosphere is also observed, it is noticed that as the O/N_2 ratio decreases due to the increase of neutral molecule N_2 in the ionosphere, which we have seen in the May and October magnetic storms, (unfortunately due to unavailability of data from TIMED it is not possible to show the O/N_2 ratio during the November magnetic storm), and the relative increase of ion and electron temperature makes ion-neutral and charge exchange reactions favourable for fast dissociative recombination, ultimately causing TEC depletion.

Furthermore, in this study, we evaluated the performance of the IRI model and found that it reproduces TEC variations reasonably well in mid-latitude and equatorial regions, particularly during the May and October storm periods. However, the model fails to accurately capture the TEC enhancement observed during the 12-13 November 2025 storm, highlighting its limitations in representing positive ionospheric storm dynamics and underscoring the need for improved modeling of storm-time ionospheric processes.

Future Motivation

Across all three geomagnetic storms, sudden increases and decreases in TEC are observed both prior to and following storm onset, particularly in the high and mid-latitude regions. These variations are primarily attributed to the formation and transport of plasma structures, such as polar patches. These plasma patches, which originate in the polar region and are transported toward mid-latitudes, consist of localized regions of enhanced and depletion in plasma density and can significantly impact radio wave propagation and navigation systems (Lukyanova 2026). Since it requires specialized large instruments to identify them, and these instruments are not widely available but only at a few specialized locations like in lower mid latitude region, and there data are not publicly available. So, as our next work, it is very important to try modeling their transport phenomena using whatever data is available.

Bibliography

Cai, Lei et al. (2026). "Ionosphere-Thermosphere Coupling in the Northern Polar Region During the May 2024 Geomagnetic Superstorm". In: *Journal of Geophysical Research: Space Physics* 131.2, e2025JA034495.

Cumnock, Judy Anne (1994). *The high latitude ionospheric convection pattern during northward interplanetary magnetic field*. The University of Texas at Dallas.

Curto, Juan José (2020). "Geomagnetic solar flare effects: A review". In: *Journal of Space Weather and Space Climate* 10, p. 27.

Farrell, Jay (2008). *Aided navigation: GPS with high rate sensors*. McGraw-Hill, Inc.

Fuller-Rowell, TJ and D Rees (1981). "A three-dimensional, time-dependent simulation of the global dynamical response of the thermosphere to a geomagnetic substorm". In: *Journal of Atmospheric and Terrestrial Physics* 43.7, pp. 701–721.

Fuselier, SA, SM Petrinec, and KJ Trattner (2000). "Stability of the high-latitude reconnection site for steady northward IMF". In: *Geophysical research letters* 27.4, pp. 473–476.

Heelis, RA and WB Hanson (1998). "Measurements of thermal ion drift velocity and temperature using planar sensors". In: *Measurement techniques in space plasmas: particles* 102, pp. 61–71.

Hofmann-Wellenhof, Bernhard, Herbert Lichtenegger, and James Collins (2012). *Global positioning system: theory and practice*. Springer Science & Business Media.

Jin, Yaqi et al. (2025). "Significant plasma density depletion from high-to mid-latitude ionosphere during the super storm in May 2024". In: *Geophysical Research Letters* 52.5, e2024GL113997.

Keidar, Michael and Isak I Beilis (2006). "Electron transport phenomena in plasma devices with E/spl times/B drift". In: *IEEE Transactions on Plasma Science* 34.3, pp. 804–814.

Kelley, Michael C (2009). *The Earth's ionosphere: Plasma physics and electrodynamics*. Vol. 96. Academic press.

Killeen, TL et al. (1984). “Ion-neutral coupling in the high-latitude F region: Evaluation of ion heating terms from Dynamics Explorer 2”. In: *Journal of Geophysical Research: Space Physics* 89.A9, pp. 7495–7508.

Kivelson, Margaret G and Christopher T Russell (1995). *Introduction to space physics*. Cambridge university press.

Koskinen, Hannu (2011). *Physics of space storms: From the solar surface to the Earth*. Springer Science & Business Media.

Lee, Wonseok et al. (2025). “Ionospheric response to the 10 May 2024 geomagnetic storm as observed in GNSS radio occultation electron density”. In: *Journal of Geophysical Research: Space Physics* 130.3, e2024JA033489.

Lukyanova, Renata (2026). “Large-scale irregularities in the high-latitude F region ionosphere represented by a numerical model, and comparison with Swarm observations”. In: *Annals of Geophysics* 69.

Misra, Pratap and Per Enge (2002). “Global positioning system: Signals, measurements, and Performance”. In: *IEEE aerospace and electronic systems magazine* 17.10, pp. 36–37.

Mitra, SK (1951). “General aspects of upper atmospheric physics”. In: *Compendium of Meteorology: Prepared under the Direction of the Committee on the Compendium of Meteorology*. Springer, pp. 245–261.

Montenbruck, Oliver, Eberhard Gill, and FH Lutze (2002). “Satellite orbits: models, methods, and applications”. In: *Appl. Mech. Rev.* 55.2, B27–B28.

Pal, Sanjoy Kumar et al. (2025). “Global response of vertical total electron content to Mother’s day G5 geomagnetic storm of May 2024: insights from IGS and GIM observations”. In: *Atmosphere* 16.5, p. 529.

Paul, Krishnendu Sekhar et al. (2025). “Effects of the October 2024 storm over the global ionosphere”. In: *Remote Sensing* 17.13, p. 2329.

Picanço, Giorgio Arlan da Silva et al. (2024). “Dynamics of Polar-Equatorial Ionospheric Irregularities During the 10-13 October 2024 Superstorm”. In: *ESS Open Archive eprints* 192, essoar–173462761.

Seemala, Gopi K. (2023). “Estimation of ionospheric total electron content (TEC) from GNSS observations”. In: *Earth Observation, Atmospheric Remote Sensing*. Ed. by A.K. Singh and S. Tiwari. Elsevier, pp. 63–84. DOI: 10.1016/B978-0-323-99262-6.00022-5.

Singh, Abhay Kumar and Shani Tiwari (2022). *Atmospheric remote sensing: principles and applications*. Elsevier.

St.-Maurice, J-P and WB Hanson (1982). “Ion frictional heating at high latitudes and its possible use for an in situ determination of neutral thermospheric winds and temperatures”. In: *Journal of Geophysical Research: Space Physics* 87.A9, pp. 7580–7602.